Effect of organic matter composition on source rock porosity during confined anhydrous thermal maturation: example of Kimmeridge-clay mudstones.

Amélie Cavelan[a,b,c*], Mohammed Boussafir[a,b,c], Claude Le Milbeau[a,b,c], Olivier Rozenbaum[d], Fatima Laggoun-Défarge[a,b,c].

(a) Université d'Orléans, ISTO, UMR 7327, 45071 Orléans, France
(b) CNRS, ISTO, UMR 7327, 45071 Orléans, France
(c) BRGM, ISTO, UMR 7327, BP 36009, 45060 Orléans, France
(d) CNRS, CEMHTI, UPR 3079, 45071 Orléans, France
* Corresponding author: amelie.cavelan@cnrs-orleans.fr

Abstract

To investigate how slight differences in the total particulate organic matter (OM) assemblage and maceral types of marine mudstones influence the development and the evolution of OM porosity throughout the same formation, laboratory gold-tube anhydrous confined thermal maturation was applied on low-mature organic-rich marine Kimmeridge clay mudstones (Yorkshire, UK). Organic petrography (palynofacies and maceral analysis), SEM observations, global and molecular geochemical characterization and low-pressure nitrogen adsorption measurements were performed to examine, to our knowledge for the first time, the role of the OM composition and properties on the evolution of porosity during thermal maturation. Evidence from organic petrography and geochemical analyses showed that organic-rich Kimmeridge clay samples containing a higher relative proportion of brown amorphous organic matter (AOM), known to be derived essentially from the cell walls of microalgae, exhibit a different pore evolution compared to samples containing a higher proportion of oil-prone orange AOM derived primarily from preservation by natural sulfurization of phytoplanktonic organic components naturally rich in lipidic compounds. OM conversion of orange AOM-rich samples has led to the production of higher amounts of low viscous oil and abundant gaseous hydrocarbon that are more favorable to the formation of abundant but small OM micropores and mesopores in the condensate/wet gas zone and less abundant large modified mineral pores in the dry gas zone. The secondary cracking of the heavier oil produced by brown-AOM-rich OM has led to the formation of a greater quantity of CO_2 and an abundant organic-rich residue more favorable to the formation of larger mesopores. Moreover, the more abundant thick laminar bituminite macerals forming a continuous ductile network particularly prone to compaction and the higher amounts of oil/bitumen generated during their conversion may have led to a higher pore collapse after oil/gas generation and migration, responsible for the destruction of part of the secondary pore network observed on some samples. Despite their slightly lower oil-prone potential, brown AOM-rich samples have thus developed larger mesopores during thermal maturation, resulting in higher pore volumes in the dry gas zone. Thus, the ability of marine mudstones to develop pores during maturation do not increase proportionally with the OM oil prone quality. These results show that variations in the individual particulate OM assemblage of a similar type II kerogen can significantly influence the amount of oil and gas generated during thermal maturation throughout the same formation, resulting in different pore evolution models. This reveals the importance of clearly identifying the composition of the original particulate OM assemblage to better predict the amount of bitumen, oil and gas generated during thermal maturation and the associated pore development.

Keywords: mudstones, porosity, maceral composition, anhydrous thermal maturation, organic petrography.

1. Introduction

The assessment of the factors influencing porosity in gas shales has become a major research focus in recent years. Mudstones (rocks containing more than 50% of grains less than 62.5 µm, Lazar et al., 2015) are mainly mesoporous (pore size as defined in Rouquerol et al., 1994) with variable amounts of macropores and micropores (Chalmers et al., 2012; Chalmers and Bustin, 2008; Mastalerz et al., 2013; Ross and Bustin, 2009). Various pore types are present including organic matter (OM) pores, interparticle and intraparticle pores associated with the mineral matrix (Loucks et al., 2012). Imaging (Curtis et al., 2012; Fishman et al., 2012; Ko et al., 2018; Loucks et al., 2012) and gas adsorption techniques (Chalmers et al., 2012; Kuila et al., 2012; Pan et al., 2015; Tian et al., 2015) revealed that OM porosity is frequently the main component of gas shales.

OM-hosted pores inherited from the original structure of cellulose, lignaceous debris or between adjacent cells of colonial algae are sometimes present (Löhr et al., 2015; Reed, 2017), but pores are rarely observed in type II OM in the immature stage (Bernard et al., 2012a; Cavelan et al., 2019; Katz and Arango, 2018; Kuila et al., 2014). However, pores are frequently observed in thermally mature mudstones (Bernard et al., 2012b; Cavelan et al., 2019; Curtis et al., 2012; Katz and Arango, 2018; Ko et al., 2018, 2016; Kuila et al., 2014; Loucks et al., 2012, 2009). It has been well-documented that changes in the abundance, size and shape of the OM pores during burial appears to be mainly stimulated by oil and primary and/or secondary gas generation from oil-prone kerogen (Bernard et al., 2012a, b; Cardott et al., 2015; Chalmers and Bustin, 2008; Chen and Xiao, 2014; Curtis et al., 2012; Katz and Arango, 2018; Ko et al., 2018, 2016; Loucks et al., 2012; Mastalerz et al., 2013; Milliken et al., 2013). However, many contradictions exist between pore evolution models in the available literature, and the relationship between mudstone porosity evolution and thermal maturity is not always clear (Katz and Arango, 2018). Previous studies show that OM pores result mainly from the secondary cracking of kerogen and bitumen within secondary solid/solidified bitumen (pyrobitumen, post-oil solid bitumen in the classification by Curiale, 1986) in response to the exsolution of gas (Bernard et al., 2012a, b; Milliken et al., 2013). This carbon-rich residue is often considered to be the main contributor to the porosity in thermally-mature mudstones (Bernard et al., 2012b; Hackley, 2017; Hackley and Cardott, 2016; Milliken et al., 2013). Romero-Sarmiento *et al.* (Romero-Sarmiento et al., 2014) suggested that these pores are present in OM because of the random reorientation and the stacking of some structural units present within OM. Keel (2015) argued that the increase in aromaticity with increasing maturity is responsible for the restructuration of OM and the formation of aromatic units surrounded by pores created during the release of gas. Nevertheless, some evidence shows that OM pores can form in the oil window within solid bitumen and/or kerogen (Juliao et al., 2015; Katz and Arango, 2018; Ko et al., 2018; Loucks et al., 2009; Reed et al., 2014).

While thermal maturation of OM and the ensuing hydrocarbon generation is considered to be the main factor controlling the development and the evolution of porosity in organic-rich mudstones (Katz and Arango, 2018), there is some evidence that the relationship between maturity and porosity may locally not be straightforward (Curtis et al., 2012; Fishman et al., 2012; Furmann et al., 2016; Guo et al., 2018; Ko et al., 2018; Löhr et al., 2015; Milliken et al., 2013; Schieber, 2010). For a given maturity, Ko *et al.* (2018) showed that two mudstones characterized by differences in maceral composition can exhibit very different pore evolution models. Other non-maturity-related factors appear to have locally a significant effect on porosity such as the organic richness (Milliken et al., 2013; Pan et al., 2015), the type or the original maceral composition of kerogen and its ability to produce oil (Cardott et al., 2015; Cardott and Curtis, 2018; Curtis et al., 2012; Guo et al., 2018; Ko et al., 2017, 2018; Loucks et al., 2012; Mastalerz et al., 2013), the nature of the rock framework and the matrix porosity (Ko et al., 2017; Milliken et al., 2013; Pan et al., 2015). However, isolating the influence of these factors on porosity during burial and thermal maturation turns out to be a complex task. The processes controlling the development and the evolution of porosity during burial and the influence of the relative proportions of individual OM components need to be clarified (Katz and Arango, 2018).

To investigate how slight variations in the composition of the total particulate organic matter (OM) assemblage and maceral types affect the evolution of the size, the distribution and the abundance of pores during thermal maturation of organic-rich marine mudstones, anhydrous confined thermal maturation experiments (600 bar) were conducted on immature Kimmeridge clay source rocks (Yorkshire, UK). As previously shown, the use of laboratory simulations can significantly reduce the complexity that exists in natural gas shales and could be a key to better understand and discriminate the influence of factors other than thermal maturity on porosity (Chen and Xiao, 2014; Ko et al., 2016, 2018; Liu et al., 2018). Six samples exhibiting slight differences in the total particulate OM assemblage were selected for these experiments. The assessment of the composition of the precursor organic material, its pore structure and its evolution with increasing thermal maturity was conducted using nitrogen adsorption measurements, organic and scanning electron microscopy (SEM) petrography, bulk geochemical characterizations (Rock-Eval, GC-TCD), palynofacies and molecular analysis. The question specifically addressed is how slight differences in the relative proportion of individual OM components and maceral types throughout the same formation affect OM pore development and evolution during maturation of organic-rich marine mudstones.

Water is commonly present within the porosity of reservoir systems and is often considered to be the main source of hydrogen during OM thermal degradation processes (Lewan, 1997). However, previous studies have demonstrated that the high temperatures used during laboratory experiments may greatly enhance the ability of water to enter the OM pore network, modifying the reactions between some organic species (Lewan, 1997; Michels et al., 1995). Under the lower temperatures (60-150°C, Tissot and Welte, 1984) of sedimentary basins, the solubility of organic compounds is limited, and a lower amount of water is thus available for hydrogen exchange reactions (Michels et al., 1995). To limit these effects which can significantly modify the processes of kerogen conversion and hence porosity evolution during thermal maturation, anhydrous artificial maturation conditions were used (no water was added with samples in gold cells for the experiments).

2. Samples and methods

2.1. Geological settings

The six samples used in the artificial thermal maturation experiments are immature organic-rich argillaceous mudstones collected from the Kimmeridge clay formation (KCF) of eastern England (Yorkshire, Fig.1). Considered to be a lateral equivalent of the main source rocks of the North Sea, this formation is one of the thickest and the most largely distributed organic-rich mudstone deposits in north-west Europe (Herbin et al., 1995; Rawson and Riley, 1982). The formation consists mainly of several hundred meters of organic-rich mudstones alternating with marls, interbedded coccoliths, and diagenetic limestones (Herbin et al., 1995; Rawson and Riley, 1982). KCF mudstones were deposited during the Late Jurassic transgression (Kimmeridgian to Tithonian) under a low energy and anoxic to suboxic conditions (Fig.2, Herbin et al., 1995). Formed during pronounced sea-level and climate fluctuations at the Milankovitch-scale, this formation is characterized by strong short-term cyclic variations with several orders in OM composition and abundance (Oschmann, 1988). The studied samples were collected from the well-documented cycle I of Marton and Ebberston boreholes in the Cleveland Basin (Fig.1, Boussafir et al., 1995a, b; Desprairies et al., 1995; Lallier-Vergès et al., 1995; Ramanampisoa and Disnar, 1994) and are low-mature (Rc < 0.50%, Ramanampisoa and Disnar, 1994). This cycle (Oschmann, 1988) is characterized by OM contents ranging from 1 to 11 wt% in Marton and from 3 to 18 wt% in Ebberston (Fig.2, (Boussafir and Lallier-Vergès, 1997; Cavelan et al., 2019; Desprairies et al., 1995). These changes occur in parallel with variations in the organic productivity and the oxygenation of the dispositional environment (Boussafir et al., 1995a, b; Boussafir and Lallier-Vergès, 1997; Lallier-Vergès et al., 1995). The organic-rich facies of the cycle (middle part, Herbin et al., 1995, Fig.2) were formed in more anoxic conditions during periods of very high primary productivity (Boussafir et al., 1995b; Boussafir and Lallier-Vergès, 1997). These rocks are characterized by a higher TOC content and relative proportion of highly oil-prone phytoplanktonic OM preserved by sulfurization (Boussafir et al., 1995b; Boussafir and Lallier-Vergès, 1997; Lallier-Vergès et al., 1995). OM in the rest of the cycle is composed of organic compounds with a lower oil generation potential (Boussafir et al., 1995b; Boussafir and Lallier-Vergès, 1997). To assess how these variations in OM composition affect the porosity of Kimmeridge clay source rocks during thermal maturation, the studied samples were selected to cover a wide range of TOC, variable maceral compositions but relatively similar mineralogy. Previous XRD analyses show that the studied samples contain similar mineralogy with 7.8-19.7 wt% of quartz, 13.8-17.6 wt% of carbonates, 52.5-54.6 wt% of clay and less than 10 wt% of pyrite, albite and gypsum (Cavelan et al., 2019). Three samples were collected in Marton borehole between 128.15 to 128.78 meters deep and three samples in Ebberston hole between 69.98 to 70.28 meters deep (Fig.2).

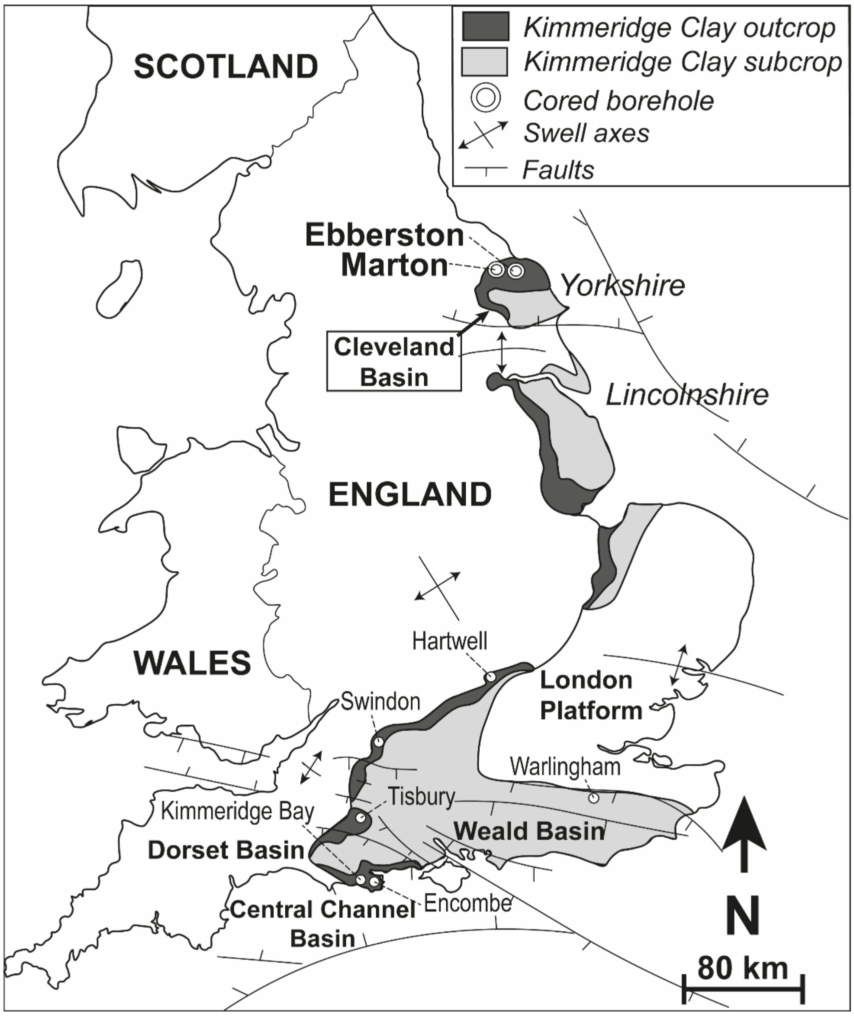

Fig.1. Location of the Kimmeridge clay formation outcrops and Marton and Ebberston holes in the Cleveland Basin, Northeast England (Yorkshire, modified from Cavelan et al., 2019; Herbin et al., 1995).

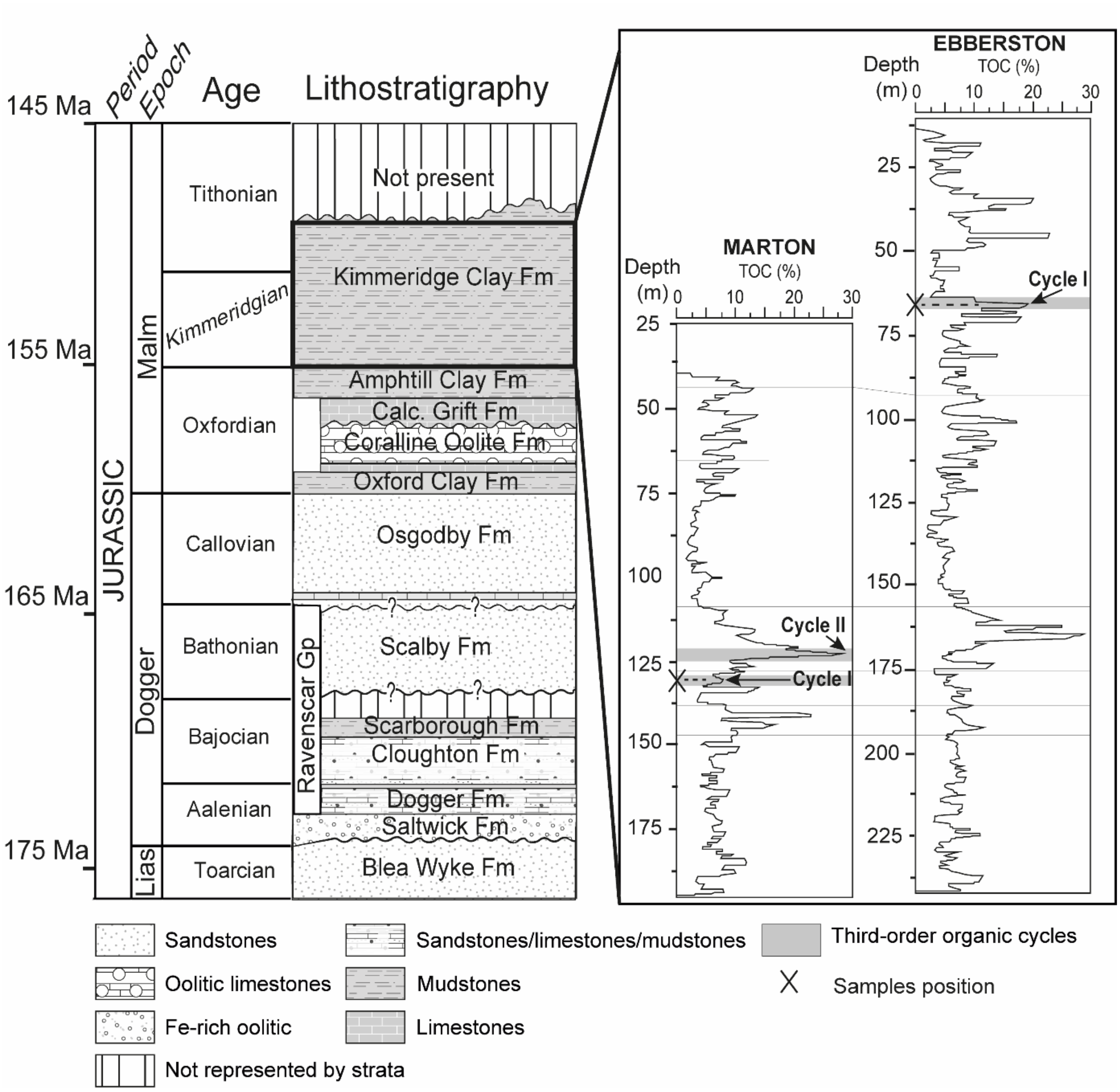

Fig.2. Simplified stratigraphic column of the Upper Jurassic in the Cleveland Basin and total organic carbon distribution with depth in Ebberston and Marton boreholes with sample locations (modified from Cavelan et al., 2019; Herbin et al., 1995; Powell, 2010).

2.2. Anhydrous gold-tube confined thermal maturation

Anhydrous gold-tube confined thermal maturation was conducted simultaneously on about 1 g of six total rocks crushed into powder (≈ 250 µm) and on a small-diameter rock cylinder (5 mm in diameter; 1.5 cm in length, drilled perpendicular to the bedding) placed and sealed under argon atmosphere inside gold cells (L = 6.5 cm, i.d = 0.5 cm, wall thickness 0.45 mm). Prior to loading the samples, open-ended tubes were heated to 550°C and washed with hydrochloric acid to remove potential organic material contaminants and the samples were dried 12 hours at 105°C to remove any potential free or adsorbed water. The cells were welded using an argon-arc welder and introduced into high-pressure stainless-steel autoclaves pressurized with water inserted into a pyrolysis oven (Fig.3). The temperature of the system was raised at 4.5°C min^{-1} to the final temperature. A hydrostatic external pressure of 600 bar was exerted on the gold cells by a system of valves connected to a pump (Fig.3). The samples were then heated under isothermal conditions at temperatures of 325°C, 390°C and 470°C for 72 hours. The temperatures used for these experiments were based on the results of Landais *et al.* (Landais et al., 1994). At the end of the run, the oven was turned off and the autoclaves were slowly depressurized to avoid the rupture of the tubes. The gold cells were then recovered and carefully cleaned with dichloromethane and sealed in separate glass bottles to collect gases.

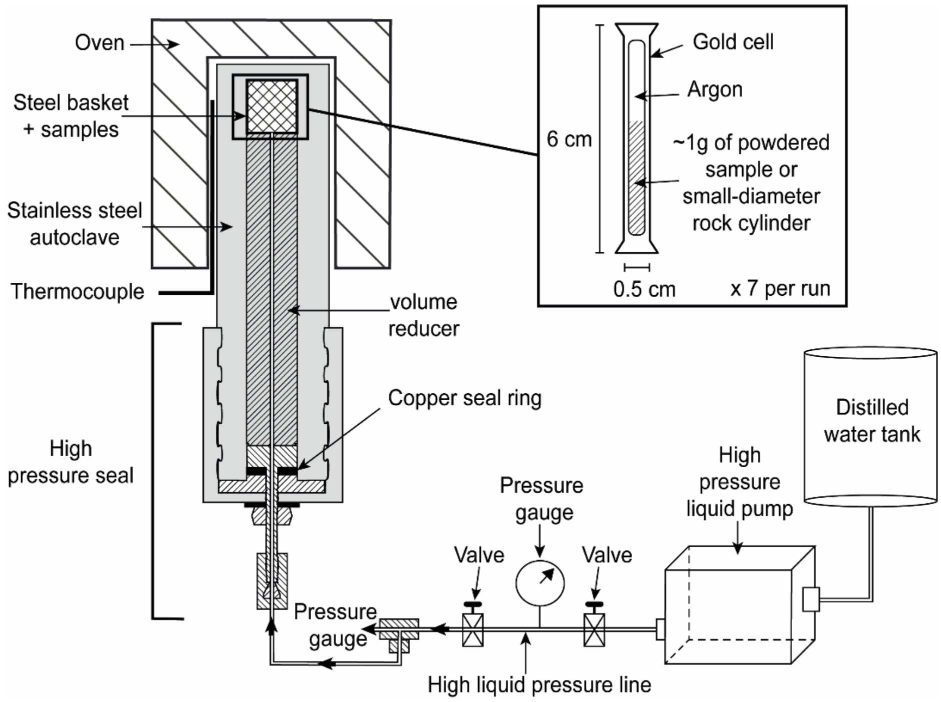

Fig.3. Laboratory anhydrous confined thermal maturation system. The high-pressure stainless-steel autoclave is held vertically during heating.

2.3. Petrography

Palynofacies analysis and quantifications were carried out on KCF isolated OM (and the associated metal sulfides) before thermal maturation using the method described elsewhere (classical HF/HCI treatment, according to Boussafir et al., 1995a). The characterization of the total OM particulate assemblage for the six studied samples was done under oil immersion using transmitted light.

Scanning electron microscope (SEM) observations and petrographic observations were then carried out under oil immersion and reflected and UV-fluorescence light (Leica® DMRX microscope) to identify the different macerals and their evolution with increasing thermal maturity. The bulk polished rock sections used for these observations were prepared as follows: the small cylinders of immature and artificially matured rocks were impregnated in epoxy resin. To facilitate broad-beam argon-ion milling, these bulk rock sections (made from the small rock cylinders only) were prepared by mechanical polishing perpendicular to bedding, first using abrasive grinding paper (up to P4000) and then alumina polishing suspensions (up to 0.04 µm). Each polished section was then argon-ion milled at 5 kV for 1 hour with a sample rotation speed set as 20 rpm and a 4° tilt rock angle and 30 min at 2 kV using a current of 220 µA (Gatan PECS model 682). Scanning electron microscope (SEM) observations were conducted using both backscatter (BSE) and secondary electron (SE) modes to image the surface texture of samples with a SEM Merlin Zeiss® equipped with an in-lens secondary electron detector at a working distance of 7.7 mm at 13 kV. Before SEM observations, the polished sections were coated with carbon and fixed to SEM stubs with a carbon paste to prevent electrostatic charging effects and improve image quality.

The estimation of the relative abundance of each type of particles observed in SEM was performed at a 1250x magnification on 12 to 15 observation areas randomly distributed all across the samples. Pore size measurements were done from zooms of these same observation areas. BSE and SE were both used during quantification to clearly discriminate OM and pores. Quantifications were done by superimposing on each observation area a 57 µm square grid divided into 36 units of 9.3*9.3 µm. The total number of units occupied by each particle type was then counted for each sample allowing the estimation of their relative abundance. The quantification was considered as affective when at least a total of 400 units were counted for each sample.

2.4. Organic geochemistry

The type, quality and amount of OM preserved in KCF samples before and after thermal maturation were determined using new Rock-Eval 6® pyrolysis (Vinci Technologies, Rueil Malmaison). About 50 to 60 mg of powdered and dried samples were used for the analysis depending on the estimated

OM contents. The pyrolysis program involved an isothermal stage at 200°C, held 2 min under inert gas (helium); the temperature was then raised to 650°C (30°C.min-^{1}) and held for 3 min. The oxidation phase started with an isothermal stage at 400°C under purified air. Then, the oven temperature was raised to 850°C (at 30°C.min^{-1}) and held for 5 min. New Rock-Eval 6$^{®}$ classical parameters and their significance were explained by Espitalie *et al*. (Espitalie et al., 1985a, b) and Lafargue *et al*. (Lafargue et al., 1998). Five parameters were used in the present study: (i) the total organic carbon content (TOC, wt%), which accounts for the quantity of OM calculated from the integration of the amount of thermo-evaporated free hydrocarbons ($S_{1\ peak}$), hydrocarbons produced by kerogen pyrolysis (S_2), S_3CO and S_3CO_2 produced by the breakdown of kerogen under inert gas and S_4CO and S_4CO_2 produced by the oxidation and the pyrolysis of residual carbon under purified air; (ii) the oxygen index (OI, mg CO_2.g^{-1} TOC), which is the oxygenated quality of OM calculated from the S_3 peak; (iii) the hydrogen index (HI, mg HC.g^{-1} TOC), which represents the amount of HC quality produced during pyrolysis (calculated from the S_2 peak); (iv) the T_{max}, which is deduced from the T_{pic} of Rock-Eval VI. T_{pic} is the temperature of the peak oil production during pyrolysis. T_{max} is often used as an OM maturity indicator (Espitalie et al., 1985a, b); (v) the production index ($PI=S_1/S_1+S_2$), an indicator of free petroleum content which naturally evolves as a function of maturity.

To analyze permanent and condensable gases (CO_2, C_1, C_2-C_4 n-alkanes), the gold tubes were pierced under vacuum in a glass bottle after maturation. 2 cm^3 of gases (at atmospheric pressure) were sampled with a gastight syringe and injected in a GC-TCD for characterization. The molecular composition of the gas produced during maturation was determined using a Perkin Elmer® Clarus 580 gas chromatograph fitted with a Supelco® Carboxen 1010 Plot® Capillary column (30 m × 0.53 mm i.d., 0.15 µm film thickness). For the analysis, the temperature was held at 35°C for 5 min and then increased at 20°C.min^{-1} to 240°C. The final isotherm was held at 240°C for 40 min. The GC-TCD was purged before each analysis with an isothermal temperature held at 240°C for 25 min to avoid any contamination between samples. Helium was the carrier gas. Samples were injected splitless with the injector temperature set at 240°C. For the identification and quantification of H_2O, CH_4, CO_2, C_2H_6, C_3H_8, C_4H_{10} and C_5H_{12} concentrations, calibration curves were made using standard gases. The total number of moles of gas was quantified assuming ideal gas behavior and using their respective peak areas on chromatograms.

To quantify and assess the evolution of saturated (SAT), aromatic (ARO) and polar (POL) hydrocarbon concentrations of each KCF sample during thermal maturation, about 1g of each powdered sample was ultrasonically extracted (7×10 min) with a mixture of dichloromethane/methanol (1/1, v/v). After centrifugation, the supernatants were combined, dried under nitrogen and weighed to determine the weight of the total extractible bitumen (EB). The extracts were desulfurized on copper and separated into SAT, ARO and POL fractions by a deactivated silica gel (5% with water) chromatography column. The SAT (saturated hydrocarbon fraction) was recovered by elution with heptane. The ARO (aromatic HC) were recovered by the subsequent elution of a mixture of heptane/toluene (3/1) and (2/2). The POL (Polar HC) were recovered by elution with methanol. After removal of the solvents, each fraction was dried under nitrogen and weighed to obtain the total extracted mass of saturated, aromatic and polar compounds. The ARO were then analyzed by Gas Chromatography-Mass Spectrometry (GC-MS) to quantify dibenzothiophenes and phenanthrenes. GC-MS was performed on a Trace-GC Ultra gas chromatograph (GC) coupled to a TSQ Quantum XLS mass spectrometer fitted with an AS 3000 auto sampler (from Thermo Scientific). The GC was equipped with a Thermo Trace-Gold 5 MS capillary column (60 m × 0.25 mm i.d, 0.25 film thickness). The GC operating conditions were as follows: temperature held at 80°C for 1 min, then increased to 120°C at 30°C.min^{-1} and from 120°C to 300°C at 3°C. min^{-1}. The final isotherm was held at 300°C over 68 min. The sample was injected in splitless mode with an injector temperature set at 280°C. Helium was the carrier gas. The mass spectrometer was operated in the electron ionization mode at 70 eV ionization energy and scanned from m/z 50 to 600. Dibenzothiophenes, phenanthrenes and their methylated derivatives were identified by comparison of their retention times and mass spectra with available published data and their concentrations were calculated accordingly using their respective peak areas in mass chromatograms. Squalane was used as internal standard. Vitrinite reflectance values (Rc) were calculated using three different ratios based on the distribution of dibenzothiophenes and phenanthrenes: the methylphenanthrene index (MPI-1), the dimethylphenanthrene ratio (DPR) and the methyldibenzothiophene ratio (MDBT) (measurement procedure in appendix 1, (Boreham et al., 1988; Radke, 1988; Radke et al., 1986). To avoid possible coelutions during chromatography, phenanthrenes and dibenzothiophenes were quantified using the area under their respective ion specific chromatograms (m/z 178+192+206 and m/z 184+198+212 respectively).

2.5. Pore volume and pore size distribution

Total pore volumes, specific surface areas and pore-size distributions (PSD) of mesopores to large micropores which are under the SEM detection limit, were measured before and after thermal maturation (before bitumen extraction) using a Quantachrome® NOVA 2200^e apparatus. The experimental conditions were as follows. Before analyses, about 1 g of each sample was powdered and degassed 24h at 105°C in a vacuum chamber to remove gaseous impurities and bound water adsorbed in clays. Then a high-purity nitrogen gas was injected into the vacuum sample cell under a low-temperature of -196.15°C. Adsorption-desorption isotherms were obtained under the relative pressure P/Po ranging from 0.003 to 0.987 with an equilibration time set at 100 s during the analyses. Specific surface areas were determined from nitrogen adsorption isotherms using the multipoint Brunauer, Emmett and Teller theory (BET) in the best linear range (with a minimum of 15 points) between the relative pressure P/Po 0.03 and 0.33 (Brunauer et al., 1938). Total pore volumes were determined after the liquid molar volume adsorbed at the relative pressure P/Po of 0.987. The detection limits for the specific surface area and the pore volume were 10^{-2} $m^2.g^{-1}$ and 10^{-4} $cm^3.g^{-1}$ respectively. To avoid tensile strength effect phenomena that could occur during desorption, PSD were determined from the adsorption isotherm using the Barrett, Johner and Halenda (BJH) method (Barrett et al., 1951). Micropore surface areas and pore volumes were determined using the T-plot method and the Harkins-Jura model (De Boer et al., 1966). To estimate the standard deviation of nitrogen adsorption results, the analysis of three samples were repeated four times. Total pore volume exhibits a mean standard deviation of ±4.2%, the specific surface area varies from ±12.2%, the mesopore volume from ±8.8%, the mesopore surface area from ±16% and the dV/dlog(r) from ±15.6%.

3. Results

3.1. Palynofacies and maceral compositions

The immature KCF mudstones are mainly composed of marine amorphous OM (≥80%, Tab.1) as described by Boussafir et al. (1995a, b). Some minor contributions of structure organic compounds (≤ 20% and < 2 wt.%) including algal megaspores, phytoplanktonic organic cell walls, pollen grains, lignaceous debris and various other debris derived from plant tissues are present (Tab.1, Fig.4D-H). In bulk-rock polished thin sections, debris of plant tissues and algal spores are represented respectively by grey-reflective non-fluorescent inertinite fragments (Fig.5A-D) and sparse brightly yellow-fluorescent *Tasmanaceae* bodies dispersed in the mineral matrix. Vitrinite and inertinite macerals appear mainly as small fragments that are not easily identifiable. Three types of amorphous organic components (AOM) were observed in palynofacies (Figs.4A-C). Orange and brown amorphous AOM are predominant (up to 84.3%, Tab.1).

Tab.1. Abundance of amorphous (AOM) and isolated structured organic compounds, total organic carbon content (TOC, wt.%), hydrogen index (HI, mg HC/g TOC), and orange /brown AOM ratio (Or/Br AOM) of immature Kimmeridge clay samples. PT: various phytoclasts including woody fragments, cuticular fragments and other plant tissues. S_p+Po: pollen grains, spores and preserved phytoplankton and algal fragments. Or AOM: orange AOM. Br AOM: brown AOM. Bl AOM: black AOM. Group (Gp) A corresponds to samples with Or/Br AOM < 2.0 while group B corresponds to samples with Or/Br AOM > 2.0. M: Marton borehole. E: Ebberston borehole. OC: organic carbon.

							Relative abundance (%)					OC contribution (in weight %)					
Sample no.	name	Depth (m)	Well	Gp	HI	TOC	Or AOM	Br AOM	Bl AOM	Sp+ Po	PT	Or AOM	Br AOM	Bl AOM	Sp+ Po	PT	Or/Br AOM
K16015	B2	128.15	M	A	418	3.0	8.4	63.5	13.8	8.1	6.2	0.3	1.9	0.4	0.2	0.2	0.2
K17001	B23	128.62	M	A	549	5.6	28.1	57.4	1.9	8.2	4.4	1.6	3.2	0.1	0.5	0.2	0.5
K16026	E19	69.98	E	A	557	10.3	42.5	34.0	3.6	5.1	14.8	4.4	3.5	0.4	0.5	1.5	1.3
K16019	B31	128.78	M	B	574	6.8	64.8	26.0	3.4	4.5	1.3	4.4	1.8	0.2	0.3	0.1	2.4
K16031	E38	70.25	E	B	599	14.5	73.0	17.8	2.0	4.6	2.6	10.5	2.6	0.3	0.7	0.4	4.0
K16032	E40	70.28	E	B	617	15.4	75.2	18.1	0.9	3.9	2.0	11.6	2.8	0.1	0.6	0.3	4.1

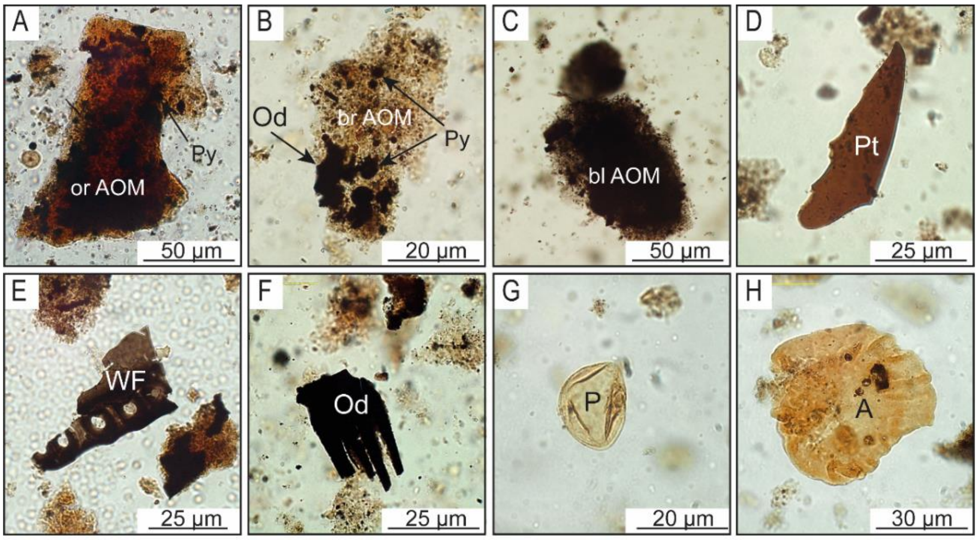

Fig.4. Various isolated amorphous (A-C) and isolated structured organic compounds (F-H) observed in the Kimmeridge clay formation before maturation (optical microscopy, transmitted light under oil immersion). A) Orange amorphous organic matter (or AOM) with pyrite inclusions (Py). B) Brown amorphous organic matter (br AOM) with oxidized debris (Od) and pyrite inclusions (Py). C) Black amorphous organic matter (bl AOM). D) Gelified membrane derived from plant tissue (Pt). E) Woody fragment (WF). F) Opaque oxidized debris derived from plant tissue (Od). G) Pollen grains (P). H) Algal fragment (A).

Previously observed in the KFC (Boussafir et al., 1995a, b), brown AOM (17.8-63.5%, Tab.1 and Fig.4B) is known to derive from the selective preservation of cell walls of microalgae and to be dispersed in the organoclay-mineral matrix. Brown AOM does not correspond to any recognizable macerals. Algal matter is also represented by abundant and discrete brightly yellowish-fluorescent elongated alginite bodies or lamellar masses (Fig.5A-D). Orange AOM (8.4-75.2% Tab.1 and Fig.4A) derives from the natural sulfurization of highly oil-prone phytoplanktonic lipidic fractions (Boussafir and Lallier-Vergès, 1997; Ramanampisoa and Disnar, 1994). In polished sections this orange AOM occurs as thick (≈10-50µm) laminar bodies with a low orange/brown fluorescence and is often associated with pyrite framboids (Fig.5A, B). Well-described in previous work on KCF (Boussafir et al., 1995b; Boussafir and Lallier-Vergès, 1997), these maceral particles are often called 'bituminites' (Kus et al., 2017). The least abundant amorphous fraction is black AOM (<14%, Tab.1 and Fig.4C) which comes from the mix of bacterial macromolecules with altered lignaceous debris (Boussafir and Lallier-Vergès, 1997).

Significant variations in the relative abundance of the organic components were observable between samples (Tab.1). A progressive increase of HI, orange AOM content and orange/brown AOM ratio (Or/Br AOM) is observed from sample B2 to E40 (Tab.1). Accordingly, to facilitate the discussion, the samples were divided in two groups (Tab.1). The limit between these groups was subjectively determined considering the orange and brown AOM relative proportions but also the general behavior of samples during thermal maturation. Note however that the OM composition evolves slightly in each group and from one group to the other. Group A corresponds to samples B2, B23 and E19 that contain a relatively lower proportion of oil-prone orange AOM (Or/Br AOM < 2.0, Tab.1), resulting in a slightly lower oil generation potential (HI<560 mg/g TOC, Tab.1). In polished sections, these samples are characterized by abundant inertinite fragments, alginite macerals and a lower amount of bituminite macerals (Fig.5C-D). Group B corresponds to samples B31, E38 and E40 which are mainly composed of oil-prone orange AOM (> 50% of TOC, Or/Br AOM > 2.0, Tab.1). Group B samples are characterized by the presence of a greater amount of bituminite in polished thin sections (Fig.5A-B).

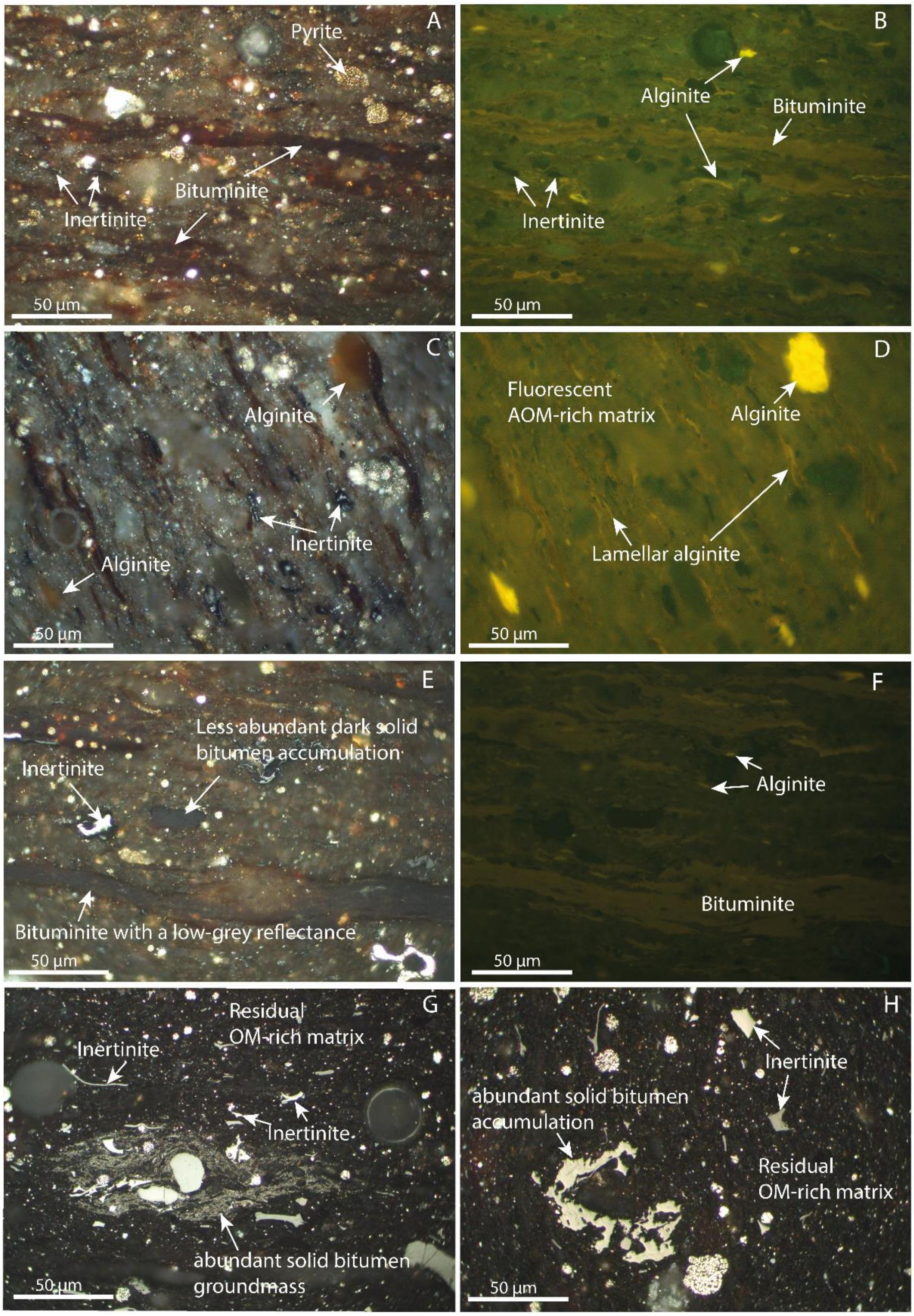

Fig.5. Photomicrographs (under oil immersion) of the Kimmeridge clay formation. A) Immature (0.48% Ro) organic-rich (TOC=14.4 wt%) mudstone of group B. C) Immature (0.46 wt%) mudstone of group A (TOC=5.6 wt%). E) Oil window (0.68% Ro) organic-rich (TOC=14.2 wt%) mudstone. G) Organic-rich (13.0 wt%) condensate-wet gas-mature sample (1.20% Ro). H) Organic-rich (5.9 wt%) dry gas-mature sample (2.50% Ro). B, D, F) Same field as A, C and E under fluorescence illumination.

After thermal maturation at 325°C for 72h, abundant highly grey-reflective solid bitumen accumulation is observable in polished sections but bituminite and alginite macerals are still predominant (Fig.5E-F). Lamellar alginite, megaspores of *Tasmanaceae* and bituminite macerals still exhibit a relatively low fluorescence (Fig.5F), suggesting that the peak of oil generation has not been reached. Some alginite and bituminite macerals exhibit a low-grey reflectance, suggesting their progressive conversion to oil (Fig.5E). After the 390°C and 470°C/72h thermal maturation runs, the maceral composition is mainly composed of highly-grey reflectance and non-fluorescent macerals identified as solid bitumen (Fig.5G-H). These macerals are known to be the predominant organic components of thermally-mature shales (Hackley, 2017; Hackley and Cardott, 2016). They mainly form an abundant groundmass or accumulations with a homogeneous or pitted surface texture (Fig.5G-H). Their abundance in samples is closely related to the original TOC content and no notable differences between samples in group A and B were observed. At these high maturity stages, some inertinite fragments are present and are dispersed in the fine mineral matrix as well as abundant pyrite framboids (Fig.5G-H).

3.2. OM geochemical characterization.

The KCF selected samples are organic-rich mudstones with TOC ranging between 3.0 and 15.4 wt% before thermal maturation (Tab.2). The Rock-Eval T_{max} is approximatively 428°C and the Rc estimated using DPR, MDBT and MPI-1 ratios exhibit similar values of ≈ 0.48% (Tab.3, measurement procedure in appendix 1). The plot of HI versus OI and S_2 values indicates the presence of a type II OM signal with an intrinsically high potential for oil generation (HI ranges from 413 to 618 mgHC/g of TOC, Tab.2, Fig.6). As expected, the free hydrocarbon content (Rock-Eval $S1 \leq 0.6$ mgHC/g of rock) and the PI (≤ 0.01) are low (Tab.2). After anhydrous thermal maturation at 325°C, 390°C and 470°C for 72 hours, samples move progressively closer to the origin of the pseudo Van-Krevelen diagram due to the strong decrease in HI (Tab.2, Fig.6). After maturation at 325°C and 390°C for 72h, T_{max} increases to ≈ 440°C and ≈ 473°C respectively (Tab.2). However, many samples exhibited a S_2 curve that was too flat to allow a correct estimate of T_{max} values after thermal maturation (Tab.2). After the 325°C, the 390°C and the 470°C/72h runs, the Rc are approximatively 0.72%, 1.24% and 2.50% indicating that the beginning of the oil window, the condensate-wet gas zone and the dry gas zone have been reached respectively (Tab.3). TOC and S_2 decrease progressively with the increase in the thermal maturation temperature (Tab.2). The increase in PI from ≈0.01 to ≈0.60 (Tab.2) indicates the rise in the quantity of thermally generated HC. The remaining hydrocarbon potential (S_2) is still relatively high after maturation at 325°C for 72 hours (S2 up to 84 mg HC/g rock, Tab.2) but it decreases strongly after maturation at 390°C/72h (S2 ≤ 26.3 mg HC/g rock) where more than 77% of the TOC is composed of residual carbon (RC, Tab.2). After maturation at 470°C for 72h, the TOC is composed of inert residual carbon without any remaining hydrocarbon potential (S2 ≤ 1.1 mg HC/g rock, Tab.2).

Tab.2. Comparison of main Rock-Eval parameters of Kimmeridge clay samples according to maturation temperatures and duration (T). TOC: total organic carbon content (wt%). S_1: free hydrocarbons (mgHC/g of rock). S_2: pyrolyzable hydrocarbons (mgHC/g of rock). Tpic: temperature of the S_2 peak (°C). T_{max} (°C): calculated after T_{pic} and ΔT_{max} resulting from the direct comparison of T_{pic} of standard (55000) and its accepted T_{max}. HI: Hydrogen Index (mgHC/g TOC). OI: Oxygen Index (mgCO$_2$/g TOC). PI: Production index (S_1/S_1+S_2). RC: Residual carbon (wt%).

Sample no.	Sp. name	Depth (m)	Well	T°C/ Time	TOC (wt%)	S_1 (mgHC/ g rock)	S_2 (mgHC/ g rock)	T_{max} (°C)	T_{pic} (°C)	HI (mgHC/ g TOC)	OI (mgCO$_2$/ g TOC)	PI	RC/ TOC
K16015	B2	128.15	Marton	/	3.0	0.1	12.4	429	471	418	20	0.01	0.64
K17001	B23	128.62	Marton		5.6	0.2	30.6	432	474	549	12	0.01	0.53
K16019	B31	128.78	Marton		6.8	0.2	38.9	431	473	574	16	0.01	0.51
K16026	E19	69.98	Ebberston		10.3	0.2	57.4	428	470	557	14	0.00	0.53
K16031	E38	70.25	Ebberston		14.4	0.5	86.4	422	464	599	15	0.01	0.49
K16032	E40	70.28	Ebberston		15.4	0.6	95.3	425	467	617	16	0.01	0.47
K17002	B2	128.15	Marton	325/ 72h	2.9	0.2	9.1	442	484	312	7	0.02	0.74
K17003	B23	128.62	Marton		5.2	0.5	24.5	442	484	468	3	0.02	0.60
K17004	B31	128.78	Marton		6.6	0.8	32.2	442	484	491	5	0.02	0.58
K17006	E19	69.98	Ebberston		10.2	1.0	48.9	442	484	478	2	0.02	0.59
K17007	E38	70.25	Ebberston		14.2	1.7	78.9	439	481	556	3	0.02	0.55
K17008	E40	70.28	Ebberston		15.2	1.5	84	438	480	553	3	0.02	0.54
K17009	B2	128.15	Marton	390/ 72h	2.2	0.4	2.0	un	un	91	9	0.17	0.90
K17010	B23	128.62	Marton		3.0	1.2	5.6	un	un	187	3	0.18	0.81
K17011	B31	128.78	Marton		3.4	1.6	5.8	un	un	171	4	0.22	0.81
K17013	E19	69.98	Ebberston		7.2	4.6	10.6	470	512	147	2	0.30	0.81
K17014	E38	70.25	Ebberston		13.0	8.1	20.2	472	514	155	1	0.29	0.81
K17015	E40	70.28	Ebberston		13.9	10.3	26.3	475	517	189	0	0.28	0.77
K17022	B2	128.15	Marton	470/ 72h	2.0	0.3	0.2	un	un	10	9	0.60	0.98
K17023	B23	128.62	Marton		2.8	0.4	0.2	un	un	8	1	0.67	0.98
K17024	B31	128.78	Marton		3.2	0.5	0.5	un	un	15	9	0.50	0.99
K17026	E19	69.98	Ebberston		7.0	0.7	0.5	un	un	7	5	0.58	0.98
K17027	E38	70.25	Ebberston		5.9	1.4	1.2	un	un	21	10	0.54	0.96
K17028	E40	70.28	Ebberston		5.4	1.1	1.4	un	un	27	11	0.44	0.95

un: unmeasurable Tmax due to a flat S_2 peak.
/: Immature samples

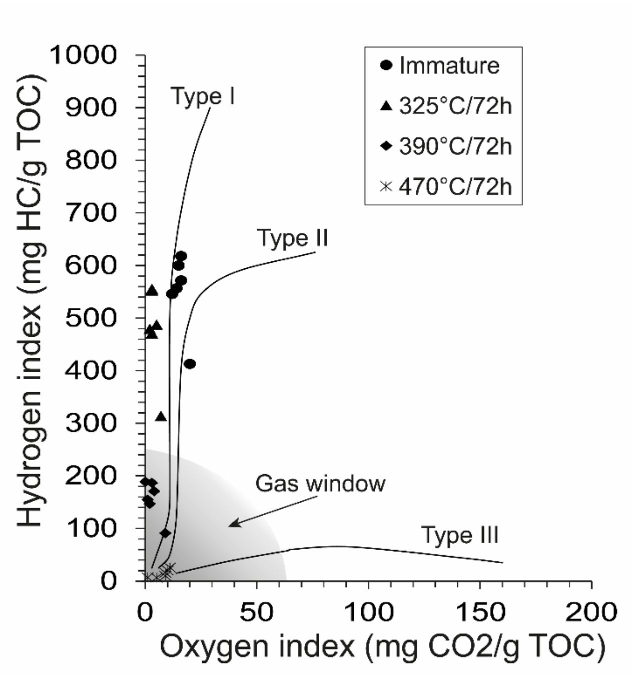

Fig.6. Pseudo-Van Krevelen diagram of Kimmeridge clay samples showing the evolution of the hydrogen (HI) and the oxygen index (OI) with increasing maturation temperatures.

Before laboratory thermal maturation, the total extractible bitumen (EB) of KCF samples was low (Tab.3, Fig.7) and mainly composed of polar compounds (73-81% of the EB, Tab.3, Fig.7). The ARO and SAT account for less than 30% (Tab.3, Fig.7). The EB content increases after maturation at 325°C for 72h for all samples as well as the concentrations of SAT and ARO compounds (Tab.3, Fig.7) indicating oil production. After thermal maturation at 325°C/72h, bitumen, and especially, SAT and ARO concentrations increase with increasing Or/Br AOM initial ratio (Tab.3, Figs.7, 8A-B). Samples of group B, especially E38 and E40, exhibit thus higher bitumen, SAT and ARO concentrations than B2 and B23 (group A, Tab.3). More than 45% of the EB of group B samples are composed of SAT and ARO while SAT and ARO accounted only for 26 to 35% of the EB in group A samples (Tab.3, Fig.7). Samples B31 (group B) and E19 (group A) exhibit similar orange AOM contents and bitumen concentrations. However, the higher brown AOM content of E19 seems responsible for the generation of lower SAT and ARO concentrations and higher amounts of POL (in mg/g TOC) than B31 during maturation (Tab.3). HC gas concentrations produced during the 325°C/72h maturation run remain relatively low for both samples (Tab.3). CO_2 is the most abundant gas produced during this maturation stage (Tab.3, Fig.7), indicating the rapid pyrolytic reaction of oxygenated compounds of OM. After maturation at 390°C and 470°C/72h concentrations of ARO, POL and SAT and thus the total concentration of EB decrease (Tab.3) while condensable gas concentrations exhibit a strong increase (Tab.3, Fig.7), indicating the conversion of oil into gas during secondary cracking. C_2-C_5 are the most abundant hydrocarbon gases produced after maturation at 390°C/72h (Tab.3). Similar or slightly lower concentrations of C_2-C_5 are generated after maturation at 390°C and 470°C for 72h (Tab.3) while C_1 concentrations increase with increasing thermal maturation temperature (Tab.3). Water is generated during thermal maturation, but the concentrations remains very low ($\leq$ 41.1 mg/g TOC, Tab.3). During gas generation, CO_2 concentrations decrease with increasing Or/Br AOM initial ratio while C_1-C_5 concentrations increase (Tab.3, Fig.8). Hence, group A samples have approximately generated 20% lower C_1-C_5 concentrations and 50% higher CO_2 concentrations during thermal maturation (Tab.3, Fig.7). Despite similar initial orange AOM content between B31 and E19, brown AOM-rich E19 (group A) has led to the formation of significantly higher CO_2 and lower C_1-C_5 concentrations in mg/g of TOC than B31 during maturation (group B, Tab.3).

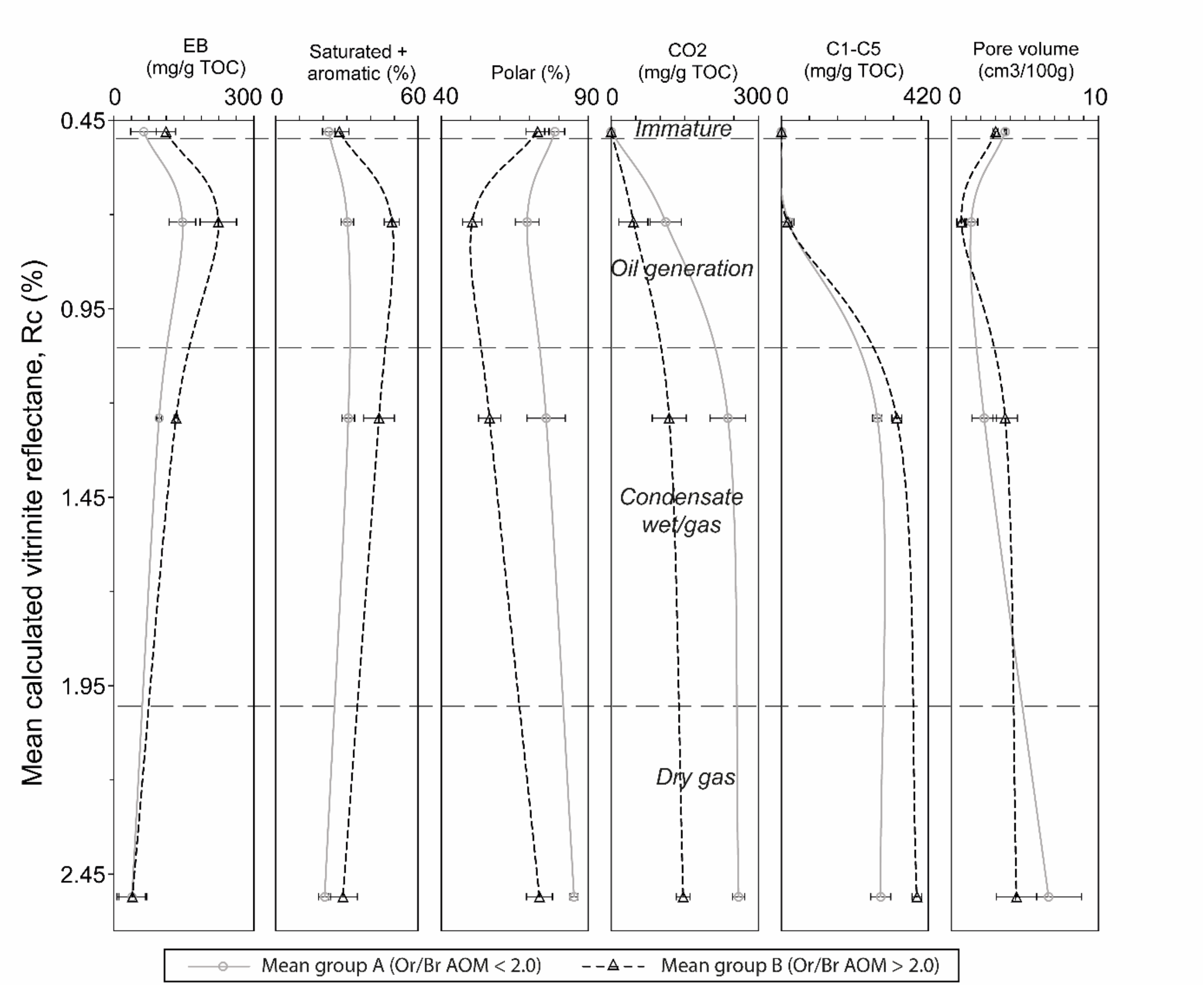

Fig.7. Evolution of group A and B mean condensable gas (CO$_2$, C$_1$-C$_5$: CH$_4$ to C$_5$H$_{12}$), total extractible bitumen (EB) concentrations, saturated, aromatic, polar hydrocarbons relative proportions and total pore volumes with increasing maturity. Group A (grey): samples with higher orange/brown amorphous organic matter ratio (Or/Br AOM< 2.0). Group B (dark): samples lower Or/Br AOM (> 2.0). Rc were estimated using the methylphenanthrene index (MPI-1), dimethylphenanthrene ratio (DPR) and methyldibenzothiophene ratio (see Tab.3).

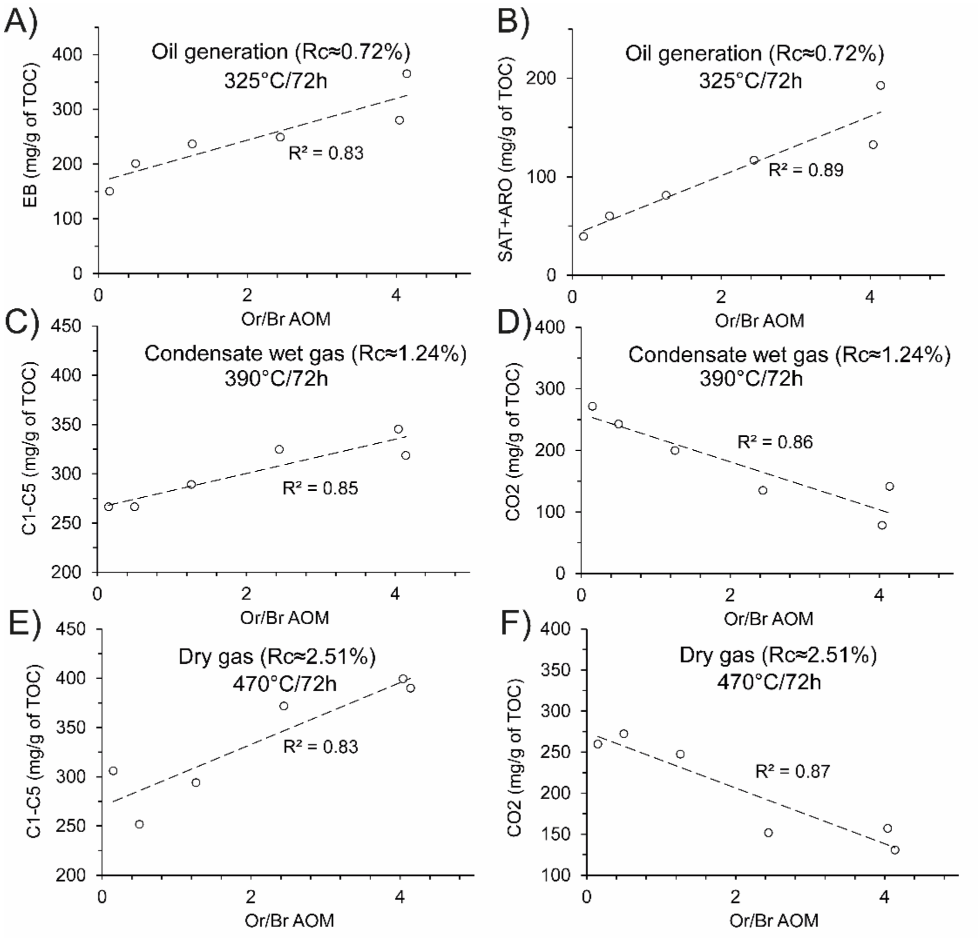

Fig.8. A-B) Plot of extractible bitumen (EB), saturated (SAT) and aromatic hydrocarbon (ARO) concentrations in the oil generation stage (325°C/72 hours) as a function of orange / brown amorphous organic matter ratios (Or/Br AOM). C-F). Plot of CO_2 and hydrocarbon gases (C_1-C_5: CH4 to C_2H_{12}) concentrations as a function of Or/Br AOM ratio after maturation at 390°C (C, D) and 470°C for 72 hours (E-F).

Tab.3. Yield (mg/g TOC) of generated condensable gases and oil components in Kimmeridge clay samples and mean calculated vitrinite reflectance values (Rc, %) determined from MDBT, DPR and MPI-1 ratios of Kimmeridge clay samples before and after maturation (for measurements, see appendix 1).

Sample no.	Sample name		MPI-1	Ro MPI-1 (%)	DPR	Ro DPR (%)	MDBT	Ro MDBT (%)	Mean Rc (%)	Rc Stand. dev.	H_2O (mg/g TOC)	CO_2 (mg/g TOC)	C_1 (mg/g TOC)	C_2-C_5 (mg/g TOC)	EB (mg/g TOC)	SAT (mg/g TOC)	ARO (mg/g TOC)	POL (mg/g TOC)	Maturity stage
K16015	B2	/	0.33	0.45	0.17	0.47	0.36	0.50	0.47	0.03	0	0	0	0	79.7	9.4	9.4	60.9	Immature
K17001	B23		0.30	0.43	0.16	0.43	0.37	0.50	0.45	0.04	0	0	0	0	51.6	5.2	7.7	38.7	
K16019	B31		0.32	0.44	0.21	0.58	0.30	0.48	0.50	0.07	0	0	0	0	124.2	6.9	16.1	101.2	
K16026	E19		0.34	0.46	0.18	0.50	0.31	0.48	0.48	0.02	0	0	0	0	117.3	8.4	18.3	90.6	
K16031	E38		0.39	0.49	0.17	0.46	0.35	0.49	0.48	0.02	0	0	0	0	167.4	25.0	26.1	116.3	
K16032	E40		0.40	0.50	0.20	0.56	0.30	0.48	0.51	0.04	0	0	0	0	162.1	17.4	26.6	118.1	
Mean			***0.35***	***0.46***	***0.18***	***0.50***	***0.33***	***0.49***	***0.48***	***0.02***									
K17002	B2	325/72h	0.82	0.79	0.27	0.74	1.19	0.64	0.72	0.08	16.6	145.8	1.2	9.3	150.2	15.8	23.7	110.7	Oil window
K17003	B23		0.74	0.74	0.28	0.76	1.21	0.64	0.71	0.06	5.3	103.6	3.2	22.1	206.0	25.1	40.2	140.7	
K17004	B31		0.73	0.73	0.30	0.80	1.45	0.67	0.73	0.07	8.1	48.0	0.6	4.2	249.1	46.7	70.1	132.4	
K17006	E19		0.81	0.79	0.28	0.76	1.50	0.68	0.74	0.06	3.1	83.6	3.1	23.5	236.7	35.2	46.0	155.5	
K17007	E38		0.70	0.71	0.26	0.72	1.40	0.67	0.70	0.03	3.3	14.7	1.9	9.1	280.3	59.9	72.8	147.7	
K17008	E40		0.56	0.61	0.29	0.78	1.22	0.65	0.68	0.09	2.3	73.5	4.4	33.7	365.1	107.7	85.2	172.3	
Mean			***0.73***	***0.73***	***0.28***	***0.76***	***1.33***	***0.66***	***0.72***	***0.05***									
K17009	B2	390/72h	1.45	1.24	0.66	1.26	5.89	1.15	1.22	0.06	5.9	271.6	21.3	245.3	122.3	6.1	18.4	97.9	Wet gas zone
K17010	B23		1.50	1.27	0.70	1.29	6.17	1.26	1.27	0.02	4.4	242.8	24.4	242.2	128.4	4.4	22.1	101.8	
K17011	B31		1.45	1.24	0.55	1.15	6.41	1.36	1.25	0.11	10.1	134.8	43.6	281.4	180.5	29.4	42.0	109.1	
K17013	E19		1.59	1.33	0.69	1.28	6.25	1.29	1.30	0.03	9.2	199.6	33.9	255.4	129.6	9.6	26.4	93.6	
K17014	E38		1.44	1.23	0.57	1.17	5.99	1.19	1.20	0.03	2.9	78.3	48.0	297.5	180.6	34.0	51.0	95.6	
K17015	E40		1.52	1.28	0.55	1.15	6.07	1.22	1.22	0.07	2.7	154.5	39.0	279.7	171.6	29.5	46.1	95.9	
Mean			***1.49***	***1.26***	***0.62***	***1.22***	***6.13***	***1.24***	***1.24***	***0.02***									
K17022	B2	470/72h	*/	*/	*/	*/	*/	*/	*/	*/	20.6	259.8	50.3	229.6	34.9	0.0	5.8	29.1	Dry gas zone
K17023	B23		*/	*/	*/	*/	*/	*/	*/	*/	6.3	272.3	33.1	215.0	20.1	0.0	2.9	17.2	
K17024	B31		0.50	2.73	3.00	2.14	8.20	2.60	2.49	0.31	9.5	144.2	94.5	277.4	20.6	2.1	4.1	14.4	
K17026	E19		0.72	2.60	5.60	2.50	8.22	2.62	2.57	0.06	41.1	297.0	54.2	229.1	100.5	3.6	10.8	86.2	
K17027	E38		0.50	2.73	4.50	2.38	7.98	2.40	2.50	0.20	21.7	157.1	106.4	272.1	58.5	4.9	9.8	43.9	
K17028	E40		0.80	2.56	4.30	2.35	8.04	2.45	2.45	0.11	22.2	171.5	122.2	261.7	87.2	5.8	17.4	64.0	
Mean			***0.63***	***2.65***	***4.35***	***2.34***	***8.11***	***2.52***	***2.51***	***0.16***									

*/ unquantifiable data due to the absence of the compounds or too low concentration. EB= extractable bitumen; SAT=saturate; ARO= aromatic; POL= polar. C_1= methane; C_2-C_5=ethane, propane, butane, pentane.

3.3. OM surface texture and pore types

3.3.1. Intra- and inter-particle mineral pores

SEM observations revealed the presence of a compact mineral structure composed mainly of quartz, pyrite framboids and carbonated microfossil remains. These minerals are surrounded by abundant clay mineral lamellar aggregates composed of sheets oriented parallel to each other (Figs.9, 10). Two types of mineral pores were observed (Fig.9).

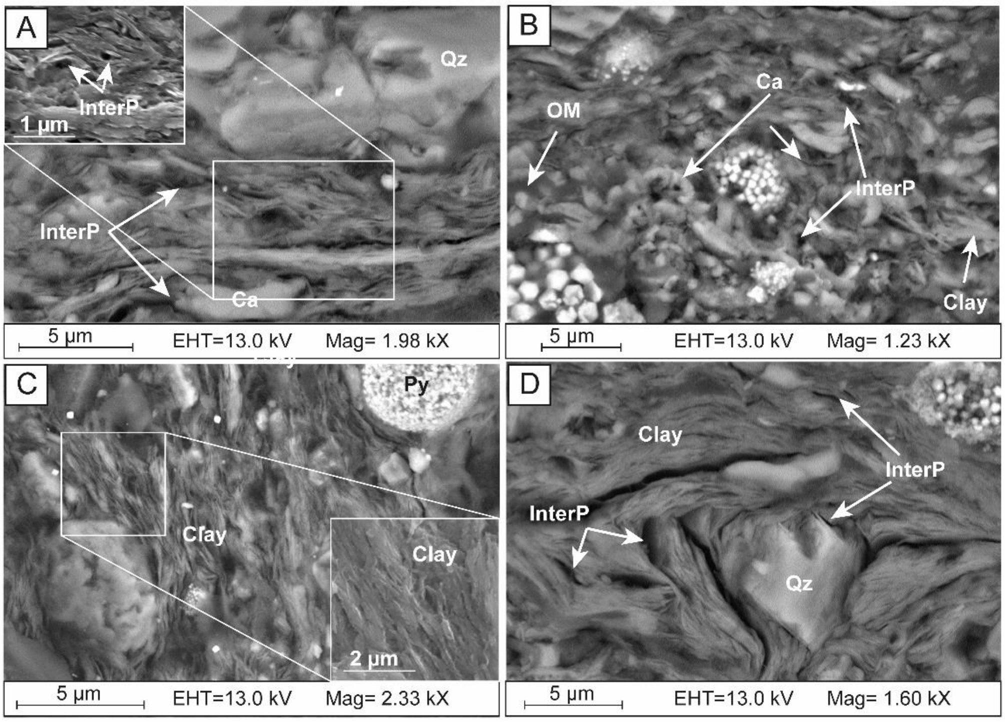

Fig.9. Scanning electron microscope BSE (A, B, C, D) and SE (inserts in A and C) images of broad ion beam milled thin sections showing examples of the predominant types of interparticle pores (InterP) present in Kimmeridge clay mudstones (mainly before thermal maturation). The length of most of these pores are below 1 µm in diameter. A) Elongated pores located between clay minerals aggregates. B) Interparticle pores located between carbonate (Ca) microfossil fragments, clay and quartz (Qz) admixture. C, D) Elongated interparticle pores located between clay minerals mineral aggregates.

The elongated intra- and interparticle pores (less than 500 nm wide and a few µm long) located within and between clay mineral sheet aggregates (Fig.9A, C, D) account for most of the porosity in immature samples (Fig.10A). Interparticle angular pores (<1 µm in diameter) located between microfossil remains, quartz and clay admixture are locally abundant in thermally immature mudstones (Fig.9B). Most of the pores observed in KCF samples before thermal maturation are inter- or intraparticle macropores associated with minerals (Figs.9, 10C). These intra and interparticle mineral pores become less abundant after thermal maturation (Fig.10). In the oil window, most of these pores have disappeared, filled by a diffuse structureless and homogeneous mass of OM which appears as a gel surrounding mineral grains (Figs.10D, 11A, B).

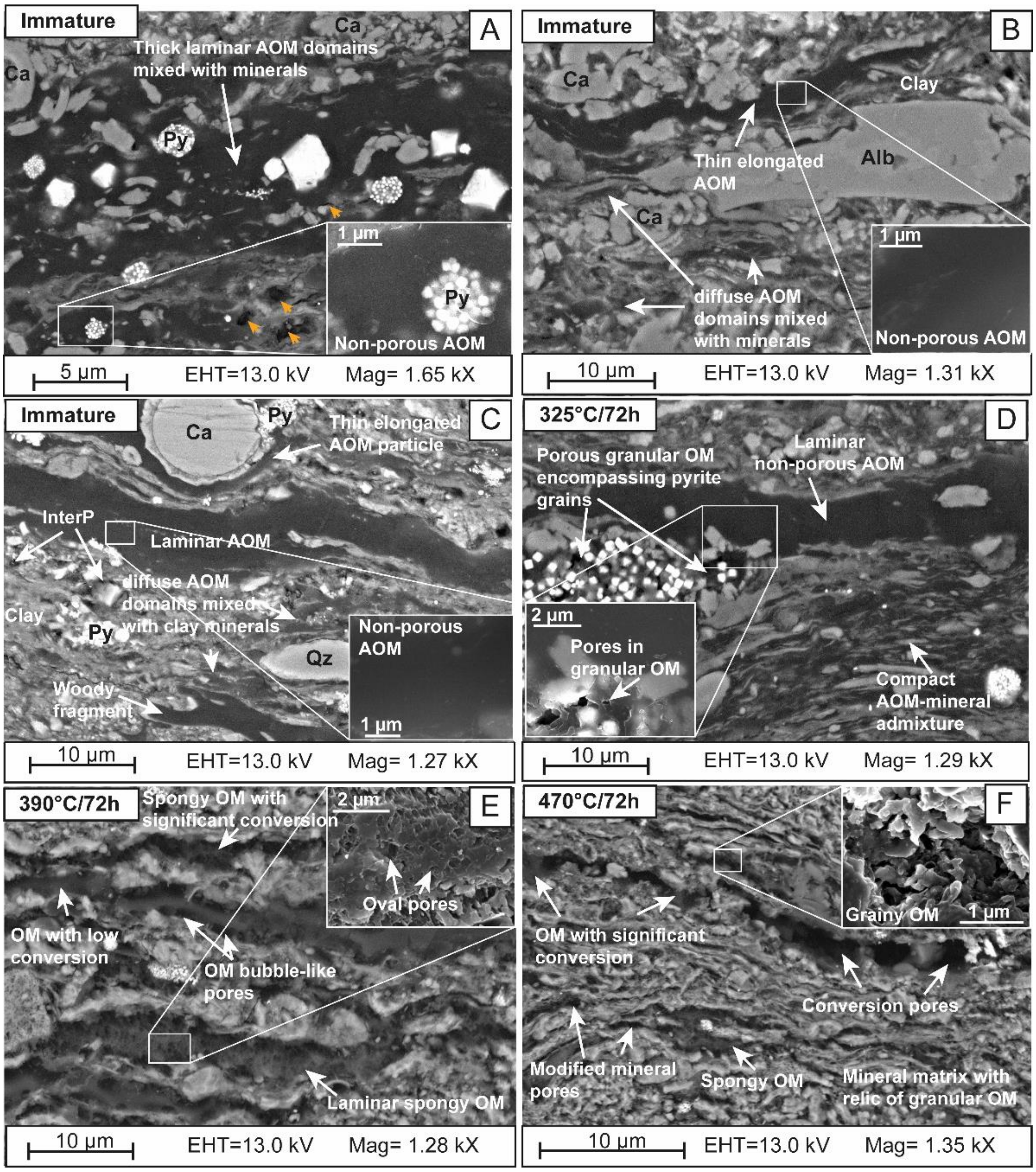

Fig.10. Scanning electron microscope BSE images of broad ion beam milled thin sections showing different types of OM particles and the evolution of the organic matter (OM) structure of organic-rich group A and group B Kimmeridge clay mudstones with increasing thermal maturity (A-C, TOC=10.3 wt%; D, TOC=10.2 wt%; E, TOC=7.2 wt%; F, TOC=7.0 wt%). A) Thick laminar non-porous and

amorphous OM (AOM) domain encompassing microfossils remains, pyrite framboids (Py) and clay minerals. The large macropores are probably artefacts from sample polishing (orange arrows). B) Thin elongated AOM particle and diffuse AOM domains mixed with clay minerals. C) Thin elongated AOM particle, thick laminar AOM particle, arcuate-shaped woody fragments, and diffuse AOM mixed in the mineral matrix. D) Laminar non-porous AOM particle nearby patches of granular porous OM which encapsulate pyrite grains. The large AOM domain mixed with clay minerals and microfossils is homogeneous and non-porous. E) Laminar particles of spongy OM containing a complex 3D interconnected pore structure composed of bubble-like pores (< 500 nm of diameter). Some non-porous laminar AOM particles contain larger oval pores (≈1µm) located at the OM edges in contact with mineral surfaces. F) Large pores located between clay mineral aggregates resulting from the extensive conversion of a laminar or a thin elongated OM particle (conversion pores). Some spongy OM particles are present. Most of the porosity is composed of modified mineral pores lined by relics of granular OM (probably solid bitumen/pyrobitumen) composed of small spheres of OM. These pores result from the migration of petroleum into the surrounding mineral pores. Ca: carbonate. Qz: quartz.

3.3.2. OM-hosted pores and surface texture

The shape and the size of OM particles vary widely (Fig.10). Four types of OM particles are commonly observed in the thermally immature samples (Fig.10A). The first type is abundant marine homogeneous and non-porous thin elongated kerogen particles, oriented parallel to the bedding (Fig.10B-C). The relative abundance of these particles decreases with the increase of the initial Or/Br AOM ratio of samples. Predominant in brown AOM-rich samples of group A but less abundant in group B samples (Tab.4), these particles may derive from algal materials (same shape and size as the lamellar alginite observed by light microscopy, Fig.5A-D) and exhibit a complete lack of primary OM-hosted porosity. Some thick (≈10-50 µm wide) AOM domains form homogeneous and non-porous laminar featureless particles embedding clay minerals, microfossil remains and especially, abundant pyrite framboids (Fig.10A). The size and the strong association of this laminar AOM with pyrite framboids suggest that these particles correspond to the bituminite macerals observed by light microscopy (Fig.5A). Less abundant in samples with low orange AOM contents (group A, Tab.4), but predominant in samples with higher orange AOM contents (group B), these particles do not exhibit any distinct morphology. Some sparse non-porous woody fragments of various shapes and sizes (2 to 20 µm long for 1-4 µm wide, Figs.10C, 11G) are observed. Most of them exhibit distinct edges with typical arcuate shapes of a woody cellular structure previously described in mudstones (Guo et al., 2018; Loucks et al., 2012; Milliken et al., 2013; Reed et al., 2014). The rest of the OM is composed of small diffuse domains of AOM particles, which do not show any distinct morphology, structure or fabric and are closely mixed with clay minerals (Fig10B, C). Contrary to the thick laminar AOM particles, no pyrite framboids are associated with these diffuse AOM-clay admixtures. Very abundant in brown AOM rich samples (group A), these diffuse AOM domains are less abundant in samples with lower brown AOM contents (group B). As previously documented (Boussafir et al., 1995a, b), these particles correspond to the brown AOM. While some rare interparticle pores are observed between OM particles, rigid grains and clay aggregates, most kerogen particles of both marine and terrestrial origin exhibit a complete lack of primary OM-hosted pores at the SEM detection limit (Fig.10A-C).

Tab.4. Mean relative abundance in SEM observations of the different types of OM in brown AOM-rich (Or/Br AOM < 2.0 group A) and orange AOM-rich (Or/Br AOM > 2.0, group B) samples before and after thermal maturation at 325°C, 390°C and 470°C for 72 hours. OM: organic matter.

Thermal maturity	Immature		Oil window (325°C/72h)		Wet gas zone (390°C/72h)		Dry gas zone (470°C/72h)	
Sample group	A	B	A	B	A	B	A	B
Inter and intraparticle mineral pores associated with clay minerals and rigid grains	predominant		rare		rare		common	
Thick non-porous laminar AOM domains encapsulating clay and pyrite	Common to abundant	Abundant to very abundant	Common to abundant	Abundant to very abundant	Rare	abundant	/	/
Thin non-porous elongated AOM and diffuse AOM domains mixed with clay minerals	very abundant	abundant	very abundant	Common to abundant	rare		/	/
Non-porous woody fragments	common		common		common		common	
AOM with isolated oval pores	/		common		common	abundant	/	
OM cracks	/		/		rare		rare	
Porous spongy OM	/		/		very abundant	common	abundant	very abundant
Granular porous OM	/		rare		very abundant	common	abundant	very abundant
Modified mineral and conversion pores with relic granular OM*	/		/		rare	rare	very abundant	rare

/: Absence of the corresponding OM/pore type. Rare: < 10%. Common: 10-20%. Abundant: 20-30%. Very abundant: 30-40%. Predominant: ≥ 40%. * : Modified mineral and conversion pores are pores located between mineral and residual OM and interpreted as mineral interparticle pores containing relics of residual granular OM (solid bitumen/pyrobitumen).

After thermal maturation at 325°C, 390°C and 470°C for 72 hours, the OM surface texture varied widely in the KCF (Tab.4, Fig.10). In the early oil generation stage, most of the pores previously related to minerals in thermally immature samples are filled by a diffuse gel-like AOM (Figs.10D, 11A-C). Some of them appear to engulf pyrite grains (Fig.11A). As suggested in previous studies (Guo et al., 2018; Ko et al., 2017, 2018; Loucks et al., 2012; Loucks and Reed, 2014; Milliken et al., 2013) these particles may correspond to migrated material resulting from kerogen conversion (bitumen, oil or pre-oil gel-like solid bitumen) probably mixed with amorphous kerogen particles. Locally, these OM particles exhibit a porous granular texture (Figs.10D, 11C). All the amorphous and structured kerogen particles exhibit an almost complete lack of OM-hosted pores considering the SEM detection limit (Fig.10D). Only some isolated bubble-like pores are observed within AOM (Fig.11A) but mainly at the edges of OM, in contact with clay mineral surfaces (Fig. 11B) or within diffuse AOM domains that appear to embed mineral grains (Fig.11C). These isolated pores, still abundant in the condensate/wet gas zone, become less common with increasing thermal maturity (Tab.4). Some cracks and large pores are sometimes observed within thick laminar AOM domains in the early oil window (Fig.11A), but they are probably artefacts from sample polishing or caused by the high vacuum used during SEM observations and may not exist in the subsurface.

In the gas window, granular and spongy macroporous OM of various shapes and sizes are more abundant (Tab.4, Fig.10E, F), indicating an intense OM-hosted pore development. OM with a granular texture appears to be composed of nanometer-scale spheres of OM separated by abundant interconnected pores which varied in size from a few dozen nanometers to one micrometer (Fig.11E, G). Some OM particles contain abundant interconnected bubble-like pores and often large devolatilization vacuoles, giving them a spongy texture (Tab.4, Figs.10E, F, 11D). While most of these OM-hosted pores are mesopores (≤ 50 nm in diameter), neighboring pores are sometimes interconnected forming larger complex 3D pore structures (Fig.11D, G). The laminar shapes of some granular and spongy AOM particles (Figs.10E, F, 11D, G) and their often strong association with pyrite (Fig.11G) framboids suggest that these particles are residual marine kerogen particles. However, the origin of most of the OM is no longer identifiable (Fig.11E). Although the OM in samples with lower Or/Br AOM ratio (group A) is largely porous with abundant spongy and granular OM, many laminar AOM particles, often associated with pyrite, are still non-porous at the SEM detection limit in samples with relatively higher Or/Br AOM ratios (Group B, Tab.4, Fig.11F). Some pores are observed between clay laminar aggregates, and mineral grains (Figs.10E, F, 11I), but are mainly lined with relic granular OM, suggesting that these pores are original mineral modified pores, filled first by petroleum which was later extracted leaving behind residual solid bitumen and smaller pores (Ko et al., 2017, 2016). These modified mineral pores, account for most of the porosity of samples with a higher relative proportion of brown AOM (group A) in the dry gas zone (Tab.4) while they are relatively rare in samples with higher orange AOM contents (group B). Locally, a few large elongated pores are visible after maturation at 470°C (Fig.10D). Often described as moldic pores in the available literature (Ko et al., 2018), these pores, called conversion pores, may result from the near total conversion of some OM particles.

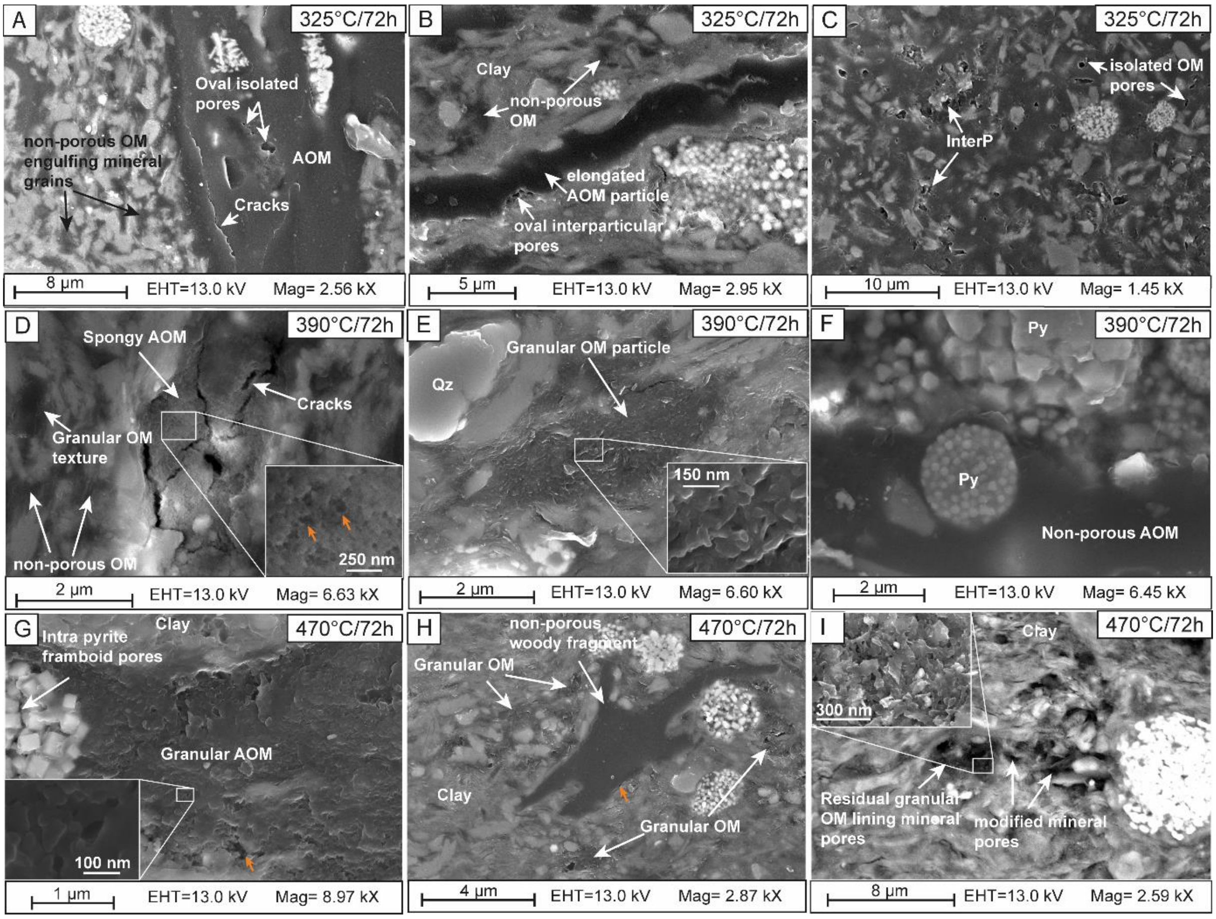

Fig.11. Scanning electron microscope SE (A-G) and BSE (H) images of broad ion beam milled thin sections showing various types of OM pores and surface texture in Kimmeridge clay mudstones. The evolution of their relative abundance with thermal maturation is shown in Tab.4 A) Amorphous organic matter (AOM) particle (probably marine kerogen) containing isolated oval pores and cracks nearby non-porous OM (probably solid bitumen) surrounded by mineral grains. B) Thin elongated non-porous AOM with convoluted edges displaying pores at the contact with mineral surfaces. C) Diffuse OM dispersed in the intergranular spaces of the mineral matrix displaying sub-angular pores and a granular surface-texture at the contact with minerals. D) Thick spongy OM particle containing abundant bubble-like pores and devolatilization cracks. Orange arrows show interconnected pores forming larger pores with a complex 3D internal structure. E) Granular AOM particle containing abundant mesopores. F) Non-porous laminar AOM associated with pyrite framboids. G) Laminar granular AOM particle containing abundant mesopores (≈ 20-100 nm) and larger interconnected pores (orange arrows) associated with a pyrite framboid. H) Non-porous woody fragment displaying the typical arcuate shape of cellular

structure. I) Modified mineral pores lined by relic granular OM (probably solid bitumen/pyrobitumen) resulting from the migration of petroleum into the surrounding mineral pores.

3.4. Nitrogen adsorption pore volume and pore size distribution

Immature KCF mudstones exhibit pore volumes and specific surface areas ranging between 2.82-3.73 cm^3/100g and 8.87-19.93 m^2/g respectively (Tab.5). The contribution of micropores is very low, with micropore volumes and specific surface areas ranging between 0.1-0.4 cm^3/100g and 0.57-7.75 m^2/g respectively (Tab.5).

Tab.5. Porosity measurements obtained using nitrogen adsorption including BET specific surface areas (S_{BET}) and total pore volumes (V_{tot}) for different maturation temperatures. V_{micro}: volume. S_{micro}: micropore specific surface area.

Sample no.	Sample name	Group	S_{BET} (m^2/g)	V_{tot} (cm^3/100g)	V_{micro} (cm^3/100g)	V_{ext} (cm^3/100g)	S_{micro} (m^2/g)	S_{ext} (m^2/g)
K16015	B2	A	19.93	3.63	0.40	3.23	6.97	12.96
K17001	B23	A	17.52	3.73	0.10	3.63	2.26	15.26
K16019	B31	B	8.87	3.01	0.30	2.71	5.72	3.15
K16026	E19	A	12.06	3.63	0.40	3.23	7.42	4.64
K16031	E38	B	10.32	2.82	0.10	2.72	1.61	8.71
K16032	E40	B	9.59	3.17	0.10	3.07	1.29	8.30
K17002	B2	A	2.35	1.35	0.10	1.25	2.05	0.30
K17003	B23	A	2.50	1.79	0.00	1.79	0.22	2.28
K17004	B31	B	1.49	1.06	0.10	0.96	0.67	0.82
K17006	E19	A	0.63	0.90	0.20	0.70	0.02	0.61
K17007	E38	B	0.85	0.49	0.00	0.49	0.11	0.74
K17008	E40	B	0.52	0.52	0.20	0.32	0.16	0.35
K17009	B2	A	3.19	1.70	0.10	1.60	1.83	1.36
K17010	B23	A	3.25	1.79	0.10	1.69	1.38	1.88
K17011	B31	B	4.12	2.97	0.20	2.77	1.00	3.12
K17013	E19	A	2.14	3.97	0.20	3.77	0.68	1.46
K17014	E38	B	7.57	3.39	0.50	2.89	3.45	4.13
K17015	E40	B	11.53	4.58	0.60	3.98	7.65	3.88
K17022	B2	A	10.30	5.33	0.20	5.13	2.79	7.51
K17023	B23	A	15.20	9.20	0.20	9.00	5.61	9.59
K17024	B31	B	6.65	3.99	0.10	3.89	1.95	4.70
K17026	E19	A	17.44	8.22	0.20	8.02	5.30	12.14
K17027	E38	B	8.12	3.32	0.00	3.31	4.72	3.40
K17028	E40	B	19.52	5.95	0.40	5.55	6.92	12.60

PSD revealed that meso and macropores ranging between 6-100 nm account for most of the pore volume (Fig.12). Mesopores and micropores in the 1.6-5.0 nm pore size range are present, but make only a low contribution to the total pore volume because of their small size (Fig.12). No clear relationships are observable between TOC, pore volume and specific surface area (Fig.13A, B). After the 325°C for 72h run, the decrease in the number of mesopores (Fig.12) leads to a strong decrease in the total pore volume ($\leq$ 1.79 cc/100g, Tab.5, Fig.7) and the specific surface area ($\leq$ 2.50 m^2/g, Tab.5) in all samples. Mesopores and macropores >10 nm account for most of the remaining pore volume (Fig.12). PSD revealed the almost complete disappearance of pores less than 10 nm (Fig.12). This thermal maturity stage is characterized by the strong decrease in the total pore volume and the specific surface area with increasing TOC (R^2=0.79 and 0.78 respectively, Fig.13C, D). Contrary to very high-TOC samples (TOC > 6 wt%), relatively low-TOC samples exhibit no real variation in the pore volume and the PSD (Tab.5, Fig.12A-B) after thermal maturation at 390°C for 72h, suggesting an influence of the organic matter content on porosity. This is substantiated by the increase in the specific surface area and pore volume (R^2=0.67 and 0.78 respectively) with TOC in these gas-mature samples (Fig.13E, F). The PSD of all group A samples (B2, B23 and E19, Or/Br AOM < 2.0) differ from group B samples (B31, E38 and E40, Or/Br AOM > 2.0, Fig.12), even between E19 and B31 which exhibit similar initial orange AOM contents. Meso and micropores in the 1.6-10 nm range account for most of the pore volume of group B samples while the pore volume of group A samples is composed of pores in the 10-100 nm pore size range (Fig.12E). No pores less than 4 nm were measured in group A (Fig.12A-C). Some pores $\geq$ 10 nm are present in group B samples, but their contribution to the pore volume is small (Fig.12E-F). After thermal maturation at 470°C for 72h, pores between 4-100 nm account for most of the pore volume (Fig.12). All samples are characterized by the almost total absence of pores less than 4 nm (Fig.12). The increase in the number of mesopores $\geq$ 4 nm increases the total pore volume in group A (Tab.5, Fig.12A-C). In group B, the increase in the number of pores in the 10-100 nm pore size range appears to partly compensate the strong decrease in the number of pores less than 8 nm (Fig.12E-F). No relationships between pore volume, specific surface area and TOC are visible at this high maturity degree (Fig.13G, H). Note that no correlation (R^2< 0.48) exist between the contents of quartz, carbonates or clay minerals previously determined (Cavelan *et al*., 2019) and the pore volume after thermal maturation.

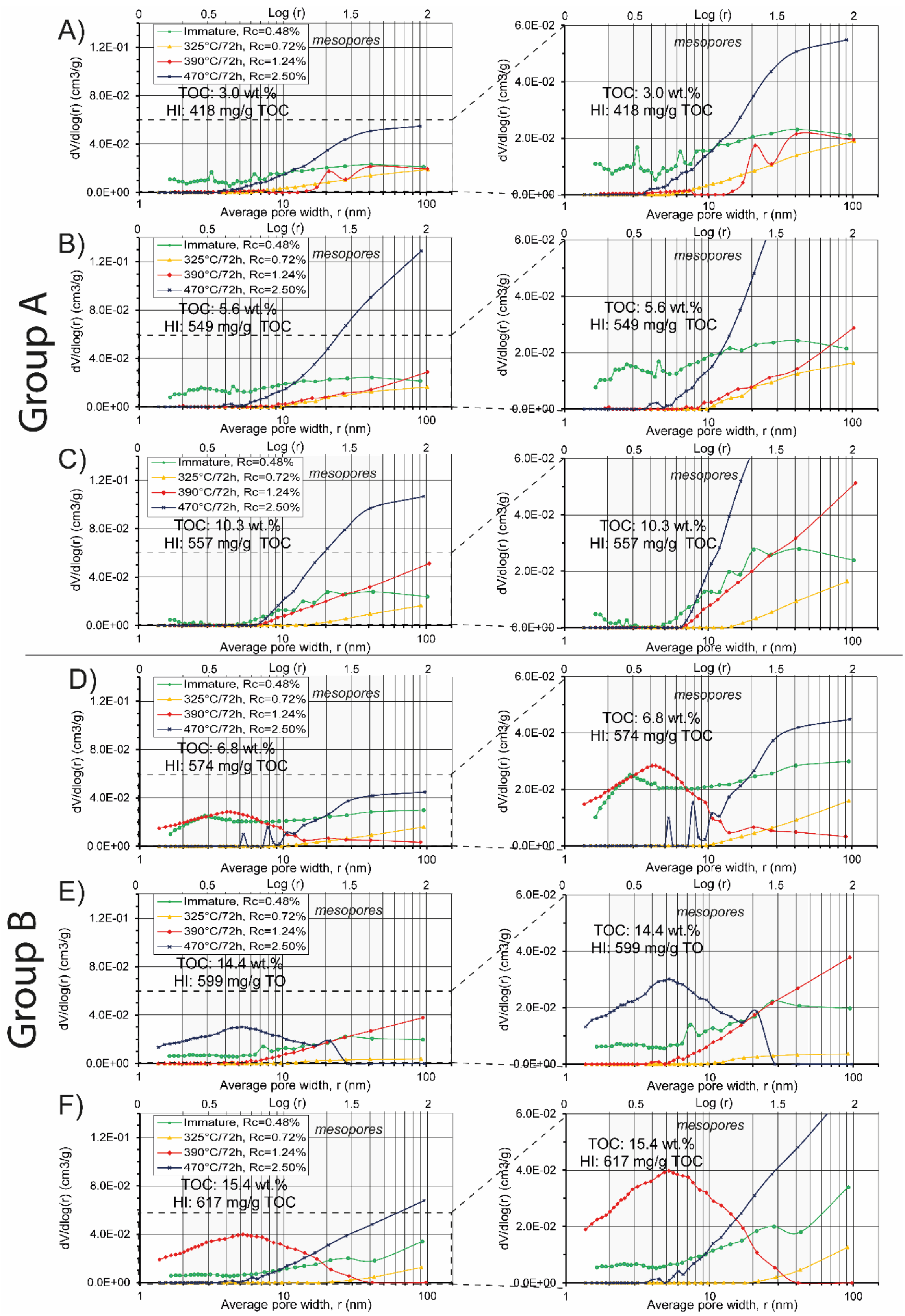

Fig.12. Comparison of pore size distribution as a function of maturation temperature, hydrogen index (HI) and the original total organic carbon content (TOC) for both sample groups. The right column shows zooms on a part of pore size distribution curves. Note that the plot of dV/dlog(r) versus r was

used to more conveniently investigate the concentration of pores of various sizes and because it represents more accurately the real contribution of pores of various sizes to the total pore volume than a common plot of the dV/dr versus r (Tian et al., 2013). Rc= mean calculated vitrinite reflectance from MPI-1, MDBT and DPR ratios.

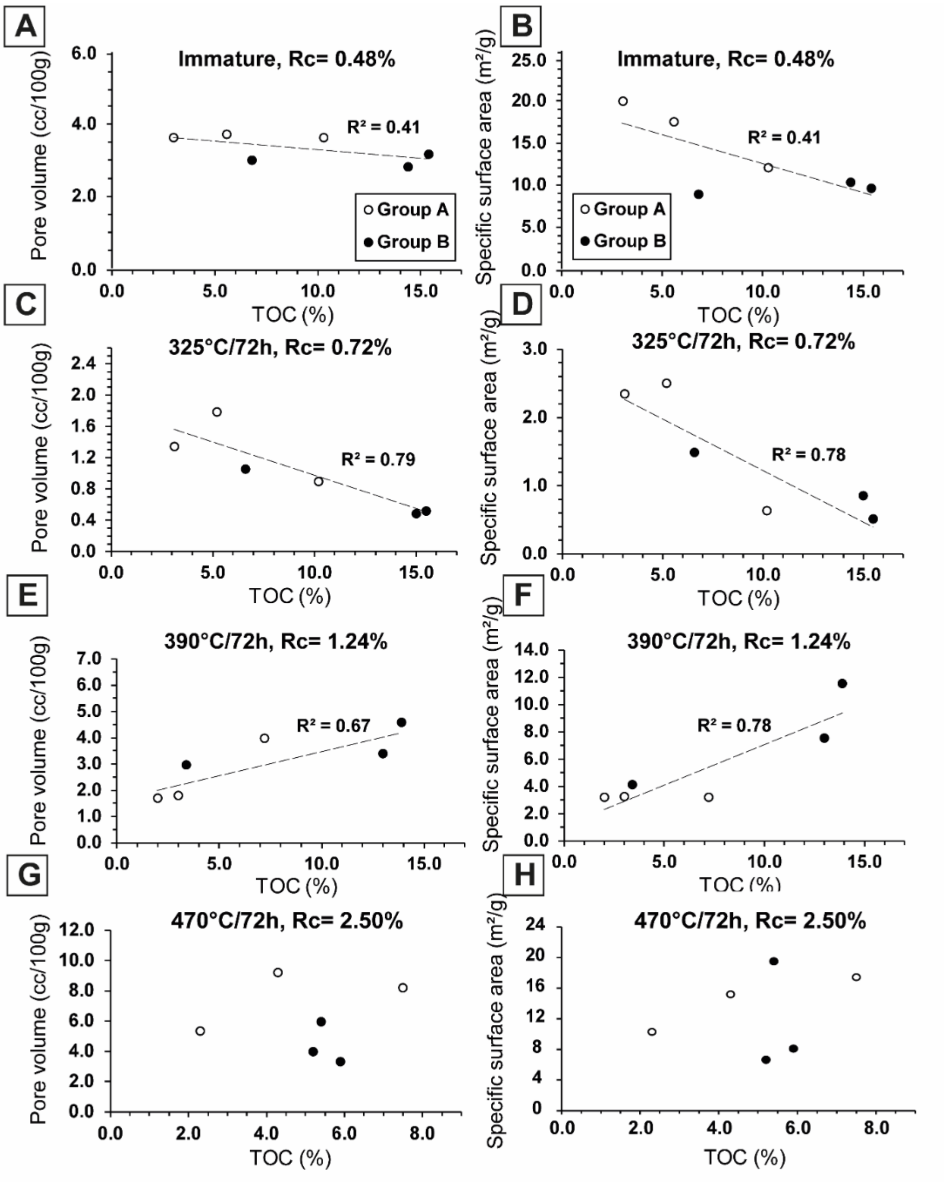

Fig.13. Variations in total pore volumes (A, C, E, G) and specific surface areas (B, D, F, H) as a function of TOC at different degrees of thermal maturity (Rc= mean calculated vitrinite reflectance from MDBT, MPI-1 and DPR ratios). Note that no correlation ($R^2 < 0.48$) exist between the contents of quartz, carbonates and clay minerals previously determined (Cavelan *et al.*, 2019) and the pore volume after thermal maturation.

4. Discussion

4.1. KCF OM texture

In accordance with previous observations (Boussafir et al., 1995b, 1995a; Boussafir and Lallier-Vergès, 1997; Cavelan et al., 2019; Lallier-Vergès et al., 1995), organic petrography, SEM and geochemical analyses reveal that KCF mudstones are composed of a well-preserved thermally immature type II kerogen with a high potential for oil generation (Tab.2, Fig.6). SEM and light optical microscopy observations reveal that KCF kerogen is composed of various components ranging from structured organic detritus with a clear precursor such as woody fragments (inertinite in light microscopy), pollen grains or algal fragments, and different types of AOM (more than 75%, Tab.1). Woody fragments can be easily identified in KCF samples by their sharp edges and their typical angular and arcuate shapes (Figs.10B, C, 11H) inherited from cell structures (Guo et al., 2018; Loucks et al., 2012; Milliken et al., 2013; Reed et al., 2014). Algal OM (lamellar alginite in reflected light microscopy) appears as thin elongated homogeneous amorphous particles in SEM images (Fig.10B, C). Brown and orange AOM (bituminite macerals in reflected light microscopy) are the most abundant types of AOM (Tab.1). Previously observed in the KCF (Boussafir et al., 1995a, b), brown AOM does not correspond to any macerals in light microscopy, and seems to be dispersed in the organoclay-mineral matrix. This marine OM is probably responsible for the high fluorescence of the mineral matrix in light microscopy (Fig.5B-D). In SEM, brown AOM appears thus, as small and diffuse AOM domains closely mixed with clay minerals (Fig.10B, C). The ultrafine structure of these particles were well studied in the KCF (Boussafir et al., 1995b). Orange AOM, which derived from the sulfurization of oil-prone hydrogen-rich phytoplanktonic components (Boussafir et al., 1995a, b; Boussafir and Lallier-Vergès, 1997) appears mainly as thick laminar particles, embedding clay minerals and pyrite framboids (Fig.10A-C).

4.2 Variations of OM compositions in the KCF

Significant variations in the relative proportion of AOM compounds responsible for slight HI variations were found between samples (Tab.1). This difference can be explained by the well-documented short-term KCF cyclic variations of OM composition (Lallier-Vergès et al., 1995; Oschmann, 1988). Pronounced changes in the depositional conditions caused by climate fluctuation at the Milankovitch-scale have greatly influenced the intensity of primary productivity and sulfate reduction processes through time (Boussafir et al., 1995a; Boussafir and Lallier-Vergès, 1997; Desprairies et al., 1995; Herbin et al., 1995; Lallier-Vergès et al., 1995; Oschmann, 1988; Ramanampisoa and Disnar, 1994). The higher orange AOM contents and HI of samples E38 and E40 (group B, Tab.1) indicate that these samples were formed during periods of relatively higher phytoplanktonic productivity and anoxic depositional conditions characterized by a significant export of metabolizable OM from the photic zone and thus a better preservation of the oil-prone metabolizable fractions of phytoplanktonic remains by sulfurization processes (Boussafir et al., 1995b; Boussafir and Lallier-Vergès, 1997; Lallier-Vergès et al., 1995). Then the progressive decrease of the primary productivity has resulted in the reduction of the phytoplanktonic OM production and export from the photic zone (Boussafir et al., 1995a; Boussafir and Lallier-Vergès, 1997; Lallier-Vergès et al., 1995). In that condition a large part of the oil-prone metabolizable OM was increasingly degraded by 'grazer' organisms (Boussafir et al., 1995a, b; Boussafir and Lallier-Vergès, 1997). Only the most resistant part of OM compounds such as resistant cell walls of green microalgae, woody and cuticular fragments (brown AOM and structured OM) may finally reach the sea bottom (Boussafir et al., 1995a, b; Boussafir and Lallier-Vergès, 1997) explaining the progressive decrease of HI and Or/Br AOM ratios from samples B31 (group B) to B2 (group A,Tab.1).

4.3. Preservation of the primary pore network in thermally immature mudstones

With a pore volume of ≈3.40 cm^3/100g (Tab.5), immature KCF samples exhibit a good original storage capacity. Nitrogen adsorption measurements reveal that samples contain pores ranging from 1.6 to 5.0 nm before thermal maturation (Fig.12). These pores make, however, a relatively low contribution to the total pore volume (Fig.12). KCF porosity before thermal maturation is mainly composed of meso- and macropores ≥6 nm (Fig.12). SEM observations show that larger macropores (mainly ≤500 nm in diameter), too large to be measured using nitrogen adsorption, are also present (Fig.9). According to SEM observations, KCF porosity is composed of inter and intraparticle pores located between rigid grains, microfossil remains and clay mineral extractible bitumen aggregates (Fig.9).

Löhr et al. (2015) showed that primary organic porosity may influence the development of secondary organic pores during thermal maturation, leading to inhomogeneity in the OM-hosted pore distribution at more elevated maturities. The presence of primary pores in originally deposited amorphous and structured OM of algal and terrestrial origin was, indeed, previously noted in various thermally immature mudstones (Han et al., 2017; Löhr et al., 2015; Mastalerz et al., 2013; Reed, 2017) including the KCF (Fishman et al., 2012; Katz and Arango, 2018). These pores, which are markedly variable even in OM of the same class, appear to be mainly derived from the original biological cell structure of particular sedimentary organic compounds or inherited from primary depositional features (Fishman et al., 2012; Löhr et al., 2015; Reed, 2017). However, as previously shown (Cavelan et al., 2019), both thermally immature marine and terrigenous kerogen particles of the studied KCF samples appear non-porous (Fig.10A-C). This well substantiates nitrogen adsorption data which show the absence of correlation between TOC, pore volume and specific surface area, suggesting no real contribution of OM-hosted pores to the total pore volume of small macropores to large micropores (Fig.13A, B). This absence of pores is not a surprise for amorphous OM particles of phytoplanktonic origin, known to have a perfect nanoscopically homogeneous ultrafine structure resulting from early diagenesis jellification processes (Boussafir et al., 1995b). While OM-hosted pores may subsist in woody fragments and amorphous OM of algal and phytoplanktonic origin, they may not survive compaction and early diagenesis processes (such as microbial reworking) in our KCF samples. Schieber (2013) suggested that primary OM-hosted pores are more likely to be preserved in the presence of a protective rigid framework of grains which can hinder OM compaction. Our KCF samples are mainly composed of ductile components such as abundant clay mineral sheets, thick laminar AOM, thin elongated AOM particles and diffuses AOM domains mixed with clay minerals (Figs.9, 10) known to be particularly prone to compaction (Fishman et al., 2012; Milliken et al., 2014). The deformation of this ductile framework may have resulted in the destruction of a potential primary OM-hosted pore network and in the migration of deformed amorphous OM in interparticle mineral-hosted pores at the origin of the AOM-mineral complex observed by SEM (Fig.10A-C).

4.4. Evolution of KCF organic matter in anhydrous confined laboratory thermal maturation

The evolution of Rock-Eval parameters, ratios of phenanthrenes and dibenzothiophenes, SAT, ARO, POL and condensable gas concentrations show that confined anhydrous maturation experiments have accurately simulated the thermal transformation of KCF marine mudstones (Tab.3, Figs.6, 7). Despite the strong increase in SAT and ARO concentrations (Fig.7) after maturation at 325°C for 72h, the high remaining HC potential of samples suggests that only the early oil generation stage (Ro≈0.72%) has been reached. This is substantiated by the relatively low T_{max} and Rc of about 440°C and 0.72% respectively (Tab.3). The strong increase in C_2-C_5 concentrations together with the decreased SAT and ARO concentrations after maturation at 390°C for 72h, indicates that the condensate/wet gas zone has been reached (Tab.3, Fig.7). This is well-substantiated by the Rc of about 1.24% and the Tmax of about 472°C (Tab.1). Lastly, the increase in C_1 concentrations and the Rc of about 2.50% (Tab.3) indicates that the dry gas zone has been reached after thermal maturation at 470°C for 72h, leaving behind a residual OM without any remaining hydrocarbon potential (low S2, residual Carbon/TOC≈1, Tab.2).

Previous work suggests that the absence of water during maturation promotes C-C bond cross linking rather than C-C bond breaking, favoring the formation of an insoluble carbon-rich residue (solid bitumen, pyrobitumen) that may significantly limit and even prevent the generation of saturated enriched oil (Lewan, 1997, 1993). The increase in EB concentrations and relative proportions of SAT and ARO indicate, however, the production of abundant oil after maturation at 325°C for 72h (Tab.3, Fig.7). Moreover, gas analysis suggests that water was generated during confined experiments (Tab.3). As previously envisaged by Behar et al. (2003) and Huang (1996) this result indicates that enough water could be produced in response to kerogen conversion during confined pyrolysis. This appears sufficient to make the system hydrous to promote kerogen conversion into oil. Nevertheless, only low quantities of water were produced, especially in the oil generation stage (Tab.3). Part of the hydrogen from water probably hydrogenated aromatic and saturated components.

4.5. Porosity evolution related to oil and gas generation and expulsion

As suggested by previous work over the past ten years (Bernard et al., 2012a, b; Chalmers and Bustin, 2008; Chen and Xiao, 2014; Curtis et al., 2012; Hackley and Cardott, 2016; Katz and Arango, 2018; Ko et al., 2018; Loucks et al., 2012; Mastalerz et al., 2013; Milliken et al., 2013), the chemical transformations of OM and the subsequent hydrocarbon generation as oil, gas and solid bitumen are accompanied by complex evolutionary trends of OM-hosted pore development. Thermal maturation of organic matter (OM) with burial is often considered as the key factor controlling the development of OM-pores in organic-rich mudstones (Bernard et al., 2012b; Katz and Arango, 2018; Ko et al., 2018; Loucks et al., 2012).

In the studied KCF mudstones, the early oil generation stage (~0.72% Ro), marked by the appearance of solid bitumen in polished sections (Fig.5E, F), is characterized by the strong decrease in the number of pores ranging from 1.6 to 100 nm, leading to lower total pore volumes and specific surface areas (Tab.2, Fig.12). PSD revealed the almost complete filling of micro and mesopores less than 10 nm in diameter by bitumen generated from the early OM conversion (Fig.12). SEM images showed that the vast majority of the intra and interparticle macropores observed in immature samples between rigid grains, and clay minerals, are also partly filled by a diffuse AOM gel-like, probably resulting from a mixture of bitumen and kerogen (Figs.10D, 11A). Unsurprisingly, samples that initially contained higher TOC and more oil-prone orange AOM produced a slightly higher quantity of oil and thus exhibit a lower number of meso and macropores in the 10-100 nm pore size range and thus, lower remaining pore volumes after the early conversion of OM (Figs.7, 12E-F, 13C, D). This phenomenon was commonly observed in mudstones at thermal maturity up to Ro=0.90% (DiStefano et al., 2016; Furmann et al., 2016; Han et al., 2017; Katz and Arango, 2018; Ko et al., 2018; Löhr et al., 2015). These results show that the early oil generation and migration appear to be sufficient to strongly limit the availability of the original mineral inter and intraparticle macro and mesoporosity. The high remaining potential of KCF mudstones after maturation at 325°C/72h (S2 up to 84 mg HC/g rock, Tab.2) suggests that these phenomena may be strongly accentuated during peak oil generation until the total occlusion of porosity. While the occlusion of pores by oil generation and migration appears to be an obvious explanation for these phenomena, previous studies suggest that pore compaction, ductile deformations and collapse of the kerogen structure resulting from increased plasticity at the more elevated temperature and/or changes in the physical and chemical properties of kerogen may also explain part of the loss of pore space in response to oil generation (Guo et al., 2018; Löhr et al., 2015).

It is commonly assumed that the formation of OM-hosted pores occurs essentially at higher levels of maturity, during gas generation, but previous work suggests that the development of organic porosity can be initiated from an Rc of about 0.70% within pre-oil solid bitumen and kerogen (Chen and Xiao, 2014; Juliao et al., 2015; Ko et al., 2018; Loucks et al., 2009). Some rare isolated bubble-like pores (Fig.11A), varying in size from a few hundred nanometers to a few micrometers, are indeed observed in KCF OM in the early oil generation stage (Fig.11A-C). Since no OM-hosted pores are observed in immature samples, some of these pores may result from petroleum generation and expulsion processes. Most of these pores are located near the interface of OM and clay minerals (Fig.11B). Phyllosilicates are known to catalyze the formation of gas prior to petroleum (Tannenbaum and Kaplan, 1985), favoring early nucleation and the escape of gas bubbles along the surface of clay minerals (Milliken et al., 2013). These OM-hosted oval pores may result from OM-clay mineral interactions responsible for the early nucleation and devolatilization of condensable gases (especially C_2-C_5 and CO_2 at this low level of maturity, Tab.3). The available literature suggests that these processes may reach a significant level at slightly higher thermal maturity levels (~0.80-0.85% Ro), where OM-hosted pores are known to develop further (Bernard et al., 2012a; Han et al., 2017; Loucks et al., 2009). Many irregular-shaped OM pores are, however, not associated with clay minerals (Fig.11C). These pores are hosted by granular OM, probably bitumen that filled intergranular spaces between various minerals such as pyrite grains (Figs.10D, 11C). This pore network may form from bitumen migration in the intergranular porosity that has partially filled the pore space allowing the trapping of water on the edges of various minerals. These different pore types are commonly observed in mudstones (Guo et al., 2018; Milliken et al., 2013). The vast majority of OM is, nevertheless, non-porous at this low level of maturity (Ro≈0.72%). OM-hosted pores remain sparse, isolated, and largely outweighed by the volume of pores filled by oil/bitumen generation or lost by collapse and compression processes. These features make them not readily accessible and prevent the adsorption of gases on pores, explaining the very low pore volumes and the almost total absence of mesopores obtained using low-pressure gas adsorption analyses (Figs.7, 12).

As commonly observed in thermally mature mudstones (Bernard et al., 2012b; Cardott et al., 2015; Chen and Xiao, 2014; Curtis et al., 2012; Hackley, 2017; Hackley and Cardott, 2016; Ko et al., 2016, 2017, 2018; Loucks et al., 2009; Reed et al., 2014), gas generation and expulsion from the end of the oil window to the wet gas zone result in the formation of abundant secondary products from oil/bitumen (Figs.7, 5E-H, solid bitumen/pyrobitumen, post-oil bitumen according to Curiale, 1986) and the re-increase in the number of macropores (Fig.10C, D), mesopores and total pore volumes (Figs.7, 12). Pores appear to be mainly hosted by OM in SEM images (Fig.10E-F, 11). This is substantiated by the positive relationship existing between TOC, pore volume and specific surface areas (Fig.13E, F). While not all the OM is porous (Fig.11F), the majority is at the SEM detection limit, indicating an intense pore development facilitated by OM transformation (Figs.10E-F, 11). Two main types of OM hosted pores are present. Many OM particles of various sizes and shapes exhibit a spongy texture characterized by the presence of abundant subrounded pores forming a complex interconnected 3D nanometer-scale pore network (≤100 nm, Figs.10D, 11D). These well-developed OM-hosted spongy pores consist probably of devolatilization vacuoles formed from the homogeneous generation and expulsion of interconnected gas bubbles when gas nucleation becomes significant (C_1, CO_2, C_2-C_5, Tab.3) or from the release of petroleum and/or water entrapped in bitumen (Ko et al., 2017; Loucks et al., 2017). Some of these pores and the large devolatilization cracks in spongy OM (Fig.11D) may, however, be artefacts accentuated by sample preparation and SEM observations under vacuum and might not exist in the subsurface (Loucks and Reed, 2014; Klaver et al., 2016). Spongy OM-hosted pores are frequently observed in various marine and lacustrine mudstones (Bernard et al., 2012b; Cavelan et al., 2019; Guo et al., 2018; Ko et al., 2016, 2017, 2018; Loucks et al., 2017; Loucks and Reed, 2014; Reed et al., 2014). While this spongy OM is often considered to be solid bitumen/pyrobitumen (Bernard et al., 2012b; Ko et al., 2017; Loucks et al., 2017; Milliken et al., 2013), the laminar shape and the thickness of some spongy particles suggests that some of them are residual marine kerogen (Figs.10E, 11D). Granular OM appears to be made up of the aggregation of small spheres of OM separated by large and complex irregular pores at the nanometer scale (Fig.11E, G). These pores may result from a more complete nucleation and interconnection of pores created by the expulsion of oil and gas bubbles in OM or may be a consequence of the formation of pores in OM particles with different compositions. However, the rearrangement of structural units within kerogen with increasing thermal maturity and oil/gas expulsion processes may greatly contribute to the appearance of spongy and granular OM-hosted pores from the oil window to the condensate/wet gas zone (Alcantar-Lopez, 2016; Romero-Sarmiento et al., 2014). Alcantar-Lopez (2016) revealed that the progressive evolution of the kerogen structure from sub-spherical units to a more rigid crosslinked nanofiber network in SEM may significantly favor the formation of pores with increasing thermal maturity. For samples containing relatively lower TOC (<6.0 wt%), these processes appear insufficient to allow the development of a large pore volume accessible for gas adsorption (Tab.5, Fig.12A, B), probably due to the poor interconnectivity of the less abundant OM pore network. Moreover, it is important to note that PSD can differ greatly between samples of group A and B, even in samples with comparable TOC contents (Fig.12B and D or C and E), suggesting that other factors unrelated to thermal maturity and OM content are at work at this maturity stage.

In the dry gas zone, the massive generation of C_1, and the still abundant production of C_2-C_5 from OM (Tab.3, Fig.7) seem to result in a massive pore development in OM (Figs.10F, 12). The almost complete conversion of some OM particles has left behind rare large conversion pores (a few µm in size, Fig.10F) while the interconnection of spongy and granular OM-hosted pores has allowed the formation of more abundant irregular complex modified mineral pores (a few µm in diameter) lined with relic spongy and granular OM, (probably solid bitumen/pyrobitumen, Fig.11I). Most of the pores seem, therefore, to be associated with primary mineral pores, filled first by bitumen, and partly freed after the expulsion of oil and gas. These pore types have been previously described in thermally-mature mudstones (Guo et al., 2018; Ko et al., 2017, 2016). The presence of this hybrid mineral-OM porosity in KCF samples may partly explain the absence of relationships between TOC, pore volume and specific surface area in the dry gas zone (Fig.13E, F). Type III kerogen, mainly composed of woody fragments, is the only type of OM which remains non-porous in thermally mature KCF mudstones (Fig.11G). Although some dry-gas mature samples exhibit a slightly higher pore volume after thermal maturation than immature samples, most of the samples exhibit similar or lower total pore volumes (Tab.5). It is important to note that thermal maturation influences the distribution of pores between mineral and OM phases rather than the total porosity of mudstones.

4.6. Influence of the original OM particulate assemblage on porosity evolution

The available literature suggests that the maceral composition of OM can influence the development of OM-hosted pores (Furmann et al., 2016; Ko et al., 2016, 2017, 2018; Liu et al., 2018; Loucks et al., 2012; Mastalerz et al., 2013). Recently, Ko *et al.* (2018) showed that changes in the OM palynomorph and maceral assemblage between Mississippian Woodford and Barnett mudstones create variations in pore development related to differences of chemical composition and generation kinetics between maceral types. No real difference of PSD is observed between KCF samples during the early oil generation stage, probably masked by the filling of the porosity by entrapped oils and bitumen (Fig.12). However, the size and the type of OM-hosted pores developed in kerogen/solid bitumen in response to gas generation and expulsion, responsible for the progressive re-increase in the pore volume in the gas window, seems dependent on the content but especially on the composition of the OM. Significant differences are indeed observed during gas generation, indicating an impact of the maceral composition of the precursor of OM on pore development. The mineralogy, relatively homogeneous between the studied samples of Marton and Ebberston boreholes (Cavelan et al., 2019) cannot explain this difference.

The amount of oil and gas generated during thermal maturation closely depends on the initial highly oil-prone orange AOM content (bituminite macerals, Figs.7, 8). KCF samples of group B, which are characterized by higher Or/Br AOM ratios, have generated thus higher amounts of oil and gaseous hydrocarbons (C_1-C_5, Tab.3, Figs.7, 8) in mg/g of TOC during thermal maturation, leading to a slightly different timing of pore evolution. Through the immature stage (i), the condensate wet/gas zone (ii) and the dry gas zone (iii), the OM texture of orange AOM-rich samples (group B, bituminite-rich samples) evolves mainly from: (i) thick non-porous laminar amorphous particles (bituminite macerals, orange AOM) forming a continuous OM framework embedding clay minerals and pyrite framboids (Figs.10A); (ii) thick laminar particles (probably bituminite) which appear as non-porous at the SEM detection limit (Fig.11F). Nitrogen adsorption measurements suggest, however, that these amorphous particles are porous, but contain abundant small mesopores and micropores less than 10 nm which are under the SEM detection limit (Fig.12E-F) responsible for the re-increase in the total pore volume; (iii) spongy and granular particles containing abundant larger meso and macropores (≥ 10 nm), probably formed from the coalescence of smaller pores (Fig.11G). Only a few large modified mineral pores are observed, resulting in a relatively low total pore volume (Tab.4, Fig.7), which remains relatively stable throughout the gas window (Fig.7). Contrary to group B samples, the OM texture of the relatively brown AOM-rich samples of group A evolve mainly from: (i) thin more dispersed elongated non-porous amorphous particles (alginite macerals) and diffuse AOM domains (brown AOM) mixed with clay minerals (Fig.10B, C); (ii) abundant spongy and granular particles forming a more interconnected pore network made up of abundant meso and macropores ($\geq$ 10 nm) whose contribution to the total pore volume depends on the OM content (Figs.10E, 11D, E, 12A-C); (iii) more abundant modified mineral meso and macropores lined with relic granular/spongy OM, probably formed from the extensive conversion of residual spongy and granular OM (conversion pores, Fig.11I). These pores are responsible for the stronger increase in total pore volume and the number of mesopores larger than 4 nm of group A samples in the dry gas zone (Figs.7, 12). Despite a higher oil-prone quality, samples containing a higher content of oil-prone orange AOM (bituminite macerals) and lower content of brown AOM thus appear to be less favorable to the formation of large mesopores during thermal maturation, resulting in slightly lower pore volume in the dry gas zone.

Different, maybe concomitant, processes can be proposed to explain this different development of OM-hosted pores, the simplified pore evolution model is shown on Fig.14: (i) the presence of smaller pores in group B samples may result from a higher pore collapse after petroleum generation and migration in the condensate wet gas zone (Fig.14C, D), facilitated by the presence of the more abundant thick laminar bituminite particles forming a continuous ductile network particularly prone to compaction and the higher amounts of oil/bitumen generated during their conversion. Similar processes of differential pore collapse were previously envisioned to explain variations of pore volume with TOC in Marcellus and Permian shales of the Lower Yangtze region (Milliken et al., 2013; Pan et al., 2015). Moreover, we can assume that fracturing and collapsing may have occurred in group B in response to the high quantity of gas generated during the dry gas zone, leading to the collapse of pores, including modified mineral pores. This phenomenon was probably significant in samples E38 and E40, which exhibit very high TOC and orange AOM contents (> 10.0 wt.%, Tab.1). The lower concentration of gas generated during maturation of samples with higher Or/Br AOM ratios, such as B2 and B23 (group A) may have limited fracturing and collapsing allowing a better preservation of porosity mainly associated with residual brown AOM particles dispersed in the clay-rich mineral matrix (Fig.14C, D). While E19 (group A) and B31 (group B) initial orange AOM contents are similar (4.4 wt.%, Tab.1), the better preservation of pores associated with residual alginite macerals and especially brown AOM during maturation, more abundant in E19 (3.5 wt.% of brown AOM, Tab.1), may explain the larger pore sizes of E19 in the condensate wet gas zone and its higher pore volume in the dry gas zone (8.22 cm3/100g, Tab.5). (ii) the higher content of well-preserved and hydrogen-rich AOM derived from phytoplankton in samples of group B allowed the production of less viscous oil (Fig.7) and probably lower amounts of solid bitumen. The secondary cracking of these compounds in the condensate/wet gas zone resulted in the production of great quantities of gaseous HC (Fig.7) that migrate, leaving behind small but abundant fine mesopores. Meanwhile, the more degraded and less oil-prone OM of group A samples produced heavier and more viscous oils, richer in polar components (Fig.7). The secondary cracking of these samples resulted in the formation of a greater quantity of CO_2 (Fig.5) and probably more abundant secondary solid bitumen more favorable to the formation of fewer but larger mesopores associated with spongy and granular particles in the condensate wet gas zone, and more abundant modified mineral pores in the dry gas zone; (iii) as suggested by Alcantar-Lopez (2016), the progressive evolution of the kerogen structure with increasing thermal maturity may significantly favor the formation of pores with increasing thermal maturity from the oil window to the dry gas zone. We can assume that the structure of several macerals, with slightly different oil generation kinetics, may evolve differently or with a slightly different timing leading to the formation of pores that differ in number and size for the same maturity level. While these variations may not be significant in natural systems, the short duration and the higher temperature of our laboratory experiments may have strongly accentuated these differences, explaining part of the difference in pore distribution between the samples of groups A and B. The strong variation of Or/Br AOM ratio, influencing both the ability of rocks to form and to preserve pores during thermal maturation, appears sufficient to strongly influence pore development during thermal maturation. Nevertheless, further investigations are needed to understand the possible relation between maceral composition, porosity and the duration of the thermal maturation experiments.

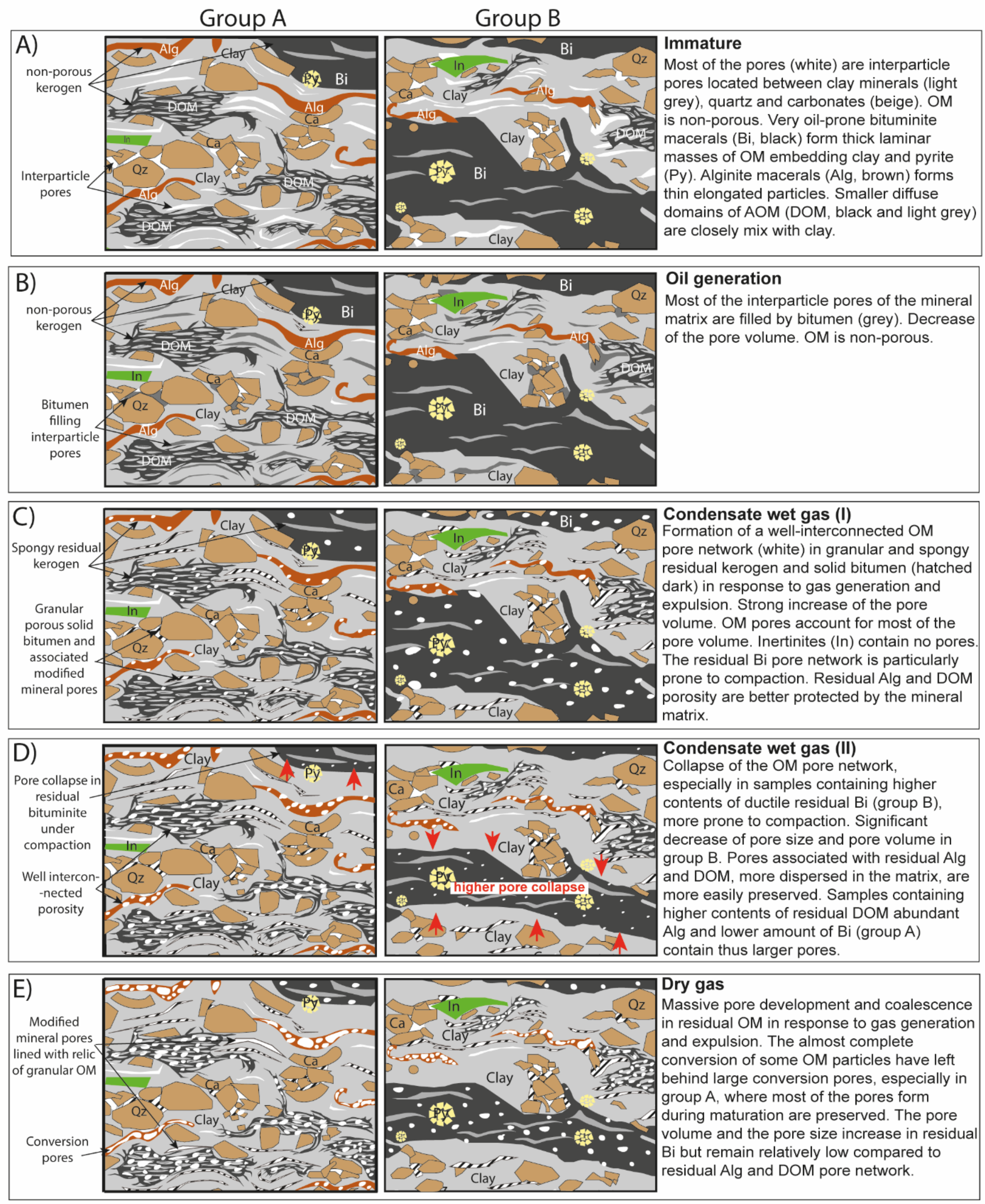

Immature
Most of the pores (white) are interparticle pores located between clay minerals (light grey), quartz and carbonates (beige). OM is non-porous. Very oil-prone bituminite macerals (Bi, black) form thick laminar masses of OM embedding clay and pyrite (Py). Alginite macerals (Alg, brown) forms thin elongated particles. Smaller diffuse domains of AOM (DOM, black and light grey) are closely mix with clay.

Oil generation
Most of the interparticle pores of the mineral matrix are filled by bitumen (grey). Decrease of the pore volume. OM is non-porous.

Condensate wet gas (I)
Formation of a well-interconnected OM pore network (white) in granular and spongy residual kerogen and solid bitumen (hatched dark) in response to gas generation and expulsion. Strong increase of the pore volume. OM pores account for most of the pore volume. Inertinites (In) contain no pores. The residual Bi pore network is particularly prone to compaction. Residual Alg and DOM porosity are better protected by the mineral matrix.

Condensate wet gas (II)
Collapse of the OM pore network, especially in samples containing higher contents of ductile residual Bi (group B), more prone to compaction. Significant decrease of pore size and pore volume in group B. Pores associated with residual Alg and DOM, more dispersed in the matrix, are more easily preserved. Samples containing higher contents of residual DOM abundant Alg and lower amount of Bi (group A) contain thus larger pores.

Dry gas
Massive pore development and coalescence in residual OM in response to gas generation and expulsion. The almost complete conversion of some OM particles have left behind large conversion pores, especially in group A, where most of the pores form during maturation are preserved. The pore volume and the pore size increase in residual Bi but remain relatively low compared to residual Alg and DOM pore network.

Fig.14. Simplified synthetic pore evolution model of Kimmeridge clay mudstones with increasing thermal maturity. Group A: samples with higher relative proportion of brown amorphous organic matter (diffuse patch of amorphous organic matter mixed with the mineral matrix: DOM). Group B: samples with higher relative proportion of orange AOM (bituminite maceral: Bi). In: inertinite fragments. Py: pyrite. Alg: alginite macerals. Ca: carbonates. Qz: quartz.

Although the OM account for less than 15 wt.% of the total KCF rocks, these results show that the initial OM composition and transformations during thermal maturation have a major effect on porosity. While pores are mainly associated with the mineral matrix in the immature samples (Cavelan et al., 2019, Fig.9), it is not true for the higher maturity stages. In migrating in the adjacent mineral pores, the significant amount of bitumen generated during thermal OM conversion, leads to a significant increase of the OM connectivity in samples and to the significant decrease of the mineral matrix pore volume (Fig.14A, B). All the interparticle pores of the mineral matrix are not filled by these secondary products but the majority does. Then, the significant volume expansion and the pressure generated during gas generation lead to the massive formation of a well interconnected pore network in the residual OM which became thus, the major contributor of the porosity of these organic-rich mudstones. While some interparticle pores of the mineral matrix are released in the form of conversion or modified mineral pores lined with relic of residual OM (Fig.10E, F), the formation of these pores closely depend on the OM conversion rate and thus on the OM composition and thermal maturity. In agreement with previous work (Bernard et al., 2012a, b; Chalmers and Bustin, 2008; Chen and Xiao, 2014; Curtis et al., 2012; Hackley and Cardott, 2016; Katz and Arango, 2018; Ko et al., 2018a; Loucks et al., 2012; Mastalerz et al., 2013; Milliken et al., 2013) all these results underscore the importance of the OM thermal degradation processes on the development of the porosity of organic-rich source rocks. Moreover, this work suggests that simply considering the amount and quality of organic matter and the level of maturity is clearly insufficient to estimate the porosity of organic-rich mudstones. As suggested by previous studies (Furmann et al., 2016; Ko et al., 2017, 2016; Liu et al., 2018; Loucks et al., 2012; Mastalerz et al., 2013; Misch et al., 2019) the relative proportion of the individual organic components, influenced by depositional and diagenetic processes, can greatly affect pore evolution during thermal maturation. Maturity appears to be the dominant factor controlling porosity. Nevertheless, non-maturity-related factors such as the chemical properties of the OM particulate assemblage, the distribution of the OM particles in the mineral matrix and the ability of the rocks to resist compaction appear to affect pore generation and development. The oil-generation potential, the behavior of the OM particulate assemblage and its generation kinetics seem to significantly influence the evolution of porosity, even within the same formation containing a similar type II kerogen. That is probably the reason why so many different trends are observed in natural gas-mudstone systems. Isolating the role of these non-maturity-related factors on pore development and evolution is an important challenge. The use of artificial maturation experiments could be a key to better understand the link between the original OM composition, the nature and the relative proportions of HC and gases generated during maturation and porosity. However, the limitations of laboratory experiments, in particular the shorter duration and the very high temperature compared to natural systems, may not appropriately simulate the effect of the OM composition on pore evolution. Comparisons with thermally mature natural samples remain necessary.

5. Summary and conclusions

To investigate how variations in the composition of the total particulate OM assemblage and maceral types throughout the same formation influence the development and the evolution of porosity during the thermal maturation of marine mudstones, laboratory gold-tube confined thermal maturation, geochemical characterization, organic petrography (SEM, palynofacies and macerals analysis), and porosimetry measurements were applied on low-mature marine Kimmeridge clay mudstones (Cleveland Basin, UK). The following conclusions can be drawn.

- The size and the distribution of pores vary greatly within Kimmeridge clay mudstones with increasing thermal maturity. The porosity of low-mature samples is mainly composed of inter and intraparticle pores located between clay aggregates and rigid grains while pores in gas-mature samples are mainly located within relics of residual granular and spongy OM.
- In migrating in the adjacent pores of the mineral matrix, the large amount of bitumen generated during oil generation, leads to a significant increase of the OM connectivity in samples and to the significant decrease of the mineral matrix pore volume. Then, the significant volume expansion and the pressure generated during gas generation lead to the massive formation of a well interconnected pore network in the residual OM, which became the major contributor of the porosity of thermally matured KCF mudstones.
- The pore space generated in kerogen/solid bitumen depends on OM content and composition. Kimmeridge clay samples containing a higher proportion of well-preserved and hydrogen-rich orange AOM derived from phytoplankton and samples containing higher relative proportions of

brown amorphous OM derived from green microalgae generated different amounts of oil/gas and exhibit a different timing of pore evolution during thermal maturation. Through the immature stage, the condensate wet/gas zone and the dry gas zone, the OM texture of orange amorphous OM-rich samples evolves mainly from: (i) thick non-porous laminar amorphous particles mixed with clay minerals and pyrite framboids; (ii) laminar particles containing very abundant small meso and micropores (≤ 10 nm) responsible for the re-increase in the total pore volume; (iii) spongy and granular particles containing abundant larger meso and macropores (≥ 10 nm), probably resulting from the coalescence of smaller pores. This does not lead to an increase in the total pore volume, which remains relatively stable throughout the gas window. The OM texture of brown amorphous OM-rich samples evolves mainly from: (i) small diffuse AOM domains mixed with clay minerals and thin elongated non-porous amorphous particles; (ii) spongy and granular particles containing abundant meso and macropores (≥ 10 nm) whose contribution to the total pore volume depends on the OM content; (iii) abundant modified mineral meso and macropores lined with relic granular/spongy OM responsible for a stronger increase in the total pore volume than for orange amorphous OM-rich samples.

- Despite their higher oil-prone quality, orange amorphous OM-rich samples developed smaller pore sizes or a small number of pores during thermal maturation, resulting in lower pore volumes in the dry gas zone. Different concomitant mechanisms may explain the smaller pores and the relatively low pore volume formed in orange amorphous OM-rich samples: (i) different variations of the orange and brown amorphous OM structure with increasing thermal maturation; (ii) a stronger framework compaction in orange amorphous OM-rich samples facilitated by the presence of a more continuous ductile framework formed by the thick laminar shape of amorphous OM and the greater volume lost during the expulsion of a greater amount of hydrocarbons; (iii) the production of less viscous oils and less abundant solid bitumens, less favorable to the formation of abundant and large meso and macropores.

Our results show that no clear positive correlation exists between the oil-prone quality of OM and its ability to develop pores during thermal maturation in these 6 investigated source rocks. Slight variations in the relative proportion of the individual organic components in the same type II kerogen can significantly influence the evolution of porosity during the thermal maturation of marine mudstones, even in the same formation. This underscores the need to clearly identify the composition of OM in order to better predict the amount of bitumen, oil and gas generated with increasing thermal maturity and the associated pore development and evolution model.

Acknowledgement

We would like to thank the anonymous reviewer for its suggestions that have greatly improved the manuscript. Special thanks go to Mrs. Elizabeth Rowley-Jolivet for her linguistic contribution. The authors would also like to thank Mrs. Ida Di Carlo for guidance on sample preparation and her expert support in the SEM BSE and SE analysis, Mr. Rémi Champallier for his help with the thermal maturation experiments, Mrs. Rachel Boscardin and Mrs. Nathalie Lottier for their assistance in the laboratory. A.Cavelan receives a PhD grant from the Region Centre-Val de Loire, France.

References

Alcantar-Lopez, L., 2016. Understanding Organic Matter Structural Changes with Increasing Thermal Maturity from Oil Shale Plays through SEM Imaging, in: Proceedings of the 4th Unconventional Resources Technology Conference. Presented at the Unconventional Resources Technology Conference, American Association of Petroleum Geologists, San Antonio, Texas, USA. https://doi.org/10.15530/urtec-2016-2456170

Barrett, E.P., Joyner, L.G., Halenda, P.P., 1951. The Determination of Pore Volume and Area Distributions in Porous Substances. I. Computations from Nitrogen Isotherms. Journal of the American Chemical Society 73, 373–380. https://doi.org/10.1021/ja01145a126

Behar, F., Lewan, M.D., Lorant, F., Vandenbroucke, M., 2003. Comparison of artificial maturation of lignite in hydrous and non hydrous conditions. Organic Geochemistry 34, 575–600. https://doi.org/10.1016/S0146-6380(02)00241-3

Bernard, S., Horsfield, B., Schulz, H.-M., Wirth, R., Schreiber, A., Sherwood, N., 2012a. Geochemical evolution of organic-rich shales with increasing maturity: A STXM and TEM study of the Posidonia Shale (Lower Toarcian, northern Germany). Marine and Petroleum Geology 31, 70–89. https://doi.org/10.1016/j.marpetgeo.2011.05.010

Bernard, S., Wirth, R., Schreiber, A., Schulz, H.-M., Horsfield, B., 2012b. Formation of nanoporous pyrobitumen residues during maturation of the Barnett Shale (Fort Worth Basin). International Journal of Coal Geology 103, 3–11. https://doi.org/10.1016/j.coal.2012.04.010

Boreham, C.J., Crick, I.H., Powell, T.G., 1988. Alternative calibration of the Methylphenanthrene Index against vitrinite reflectance: Application to maturity measurements on oils and sediments. Organic Geochemistry 12, 289–294. https://doi.org/10.1016/0146-6380(88)90266-5

Boussafir, Gelin, F., Lallier-Vergès, E., Derenne, S., Bertrand, P., Largeau, C., 1995a. Electron microscopy and pyrolysis of kerogens from the Kimmeridge Clay Formation, UK: Source organisms, preservation processes, and origin of microcycles. Geochimica et Cosmochimica Acta 59, 3731–3747. https://doi.org/10.1016/0016-7037(95)00273-3

Boussafir, Lallier-Vergès, E., Bertrand, P., Badaut-Trauth, D., 1995b. SEM and TEM studies on isolated organic matter and rock microfacies from a short-term organic cycle of the Kimmeridge Clay Formation (Yorkshire, G.B.), in: Organic Matter Accumulation. Springer Berlin Heidelberg, Berlin, Heidelberg, pp. 15–30. https://doi.org/10.1007/BFb0117665

Boussafir, Lallier-Vergès, E., 1997. Accumulation of organic matter in the Kimmeridge Clay formation (KCF): an update fossilisation model for marine petroleum source-rocks. Marine and Petroleum Geology 14, 75–83. https://doi.org/10.1016/S0264-8172(96)00050-5

Brunauer, S., Emmett, P.H., Teller, E., 1938. Adsorption of Gases in Multimolecular Layers. Journal of the American Chemical Society 60, 309–319. https://doi.org/10.1021/ja01269a023

Cardott, B.J., Curtis, M.E., 2018. Identification and nanoporosity of macerals in coal by scanning electron microscopy. International Journal of Coal Geology 190, 205–217. https://doi.org/10.1016/j.coal.2017.07.003

Cardott, B.J., Landis, C.R., Curtis, M.E., 2015. Post-oil solid bitumen network in the Woodford Shale, USA — A potential primary migration pathway. International Journal of Coal Geology 139, 106–113. https://doi.org/10.1016/j.coal.2014.08.012

Cavelan, A., Boussafir, M., Rozenbaum, O., Laggoun-Défarge, F., 2019. Organic petrography and pore structure characterization of low-mature and gas-mature marine organic-rich mudstones: Insights into porosity controls in gas shale systems. Marine and Petroleum Geology 103, 331–350.

Chalmers, G.R., Bustin, R.M., Power, I.M., 2012. Characterization of gas shale pore systems by porosimetry, pycnometry, surface area, and field emission scanning electron microscopy/transmission electron microscopy image analyses: Examples from the Barnett, Woodford, Haynesville, Marcellus, and Doig units. AAPG Bulletin 96, 1099–1119. https://doi.org/10.1306/10171111052

Chalmers, G.R.L., Bustin, R.M., 2008. Lower Cretaceous gas shales in northeastern British Columbia, Part I: geological controls on methane sorption capacity. Bulletin of Canadian Petroleum Geology 56, 1–21. https://doi.org/10.2113/gscpgbull.56.1.1

Chen, J., Xiao, X., 2014. Evolution of nanoporosity in organic-rich shales during thermal maturation. Fuel 129, 173–181. https://doi.org/10.1016/j.fuel.2014.03.058

Curiale, J.A., 1986. Origin of solid bitumens, with emphasis on biological marker results. Organic Geochemistry 10, 559–580. https://doi.org/10.1016/0146-6380(86)90054-9

Curtis, M.E., Cardott, B.J., Sondergeld, C.H., Rai, C.S., 2012. Development of organic porosity in the Woodford Shale with increasing thermal maturity. International Journal of Coal Geology 103, 26–31. https://doi.org/10.1016/j.coal.2012.08.004

De Boer, J.H., Lippens, B.C., Linsen, B.G., Broekhoff, J.C.P., Van den Heuvel, A., Osinga, T.J., 1966. Thet-curve of multimolecular N2-adsorption. Journal of Colloid and Interface Science 21, 405–414.

Desprairies, A., Bachaoui, M., Ramdani, A., Tribovillard, N., 1995. Clay diagenesis in organic-rich cycles from the Kimmeridge Clay Formation of Yorshire (G.B.): implication for palaeoclimatic interpretations, in: Organic Matter Accumulation. Springer Berlin Heidelberg, Berlin, Heidelberg, pp. 63–91. https://doi.org/10.1007/BFb0117668

DiStefano, V.H., McFarlane, J., Anovitz, L.M., Stack, A.G., Gordon, A.D., Littrell, K.C., Chipera, S.J., Hunt, R.D., Lewis, S.A., Hale, R.E., Perfect, E., 2016. Extraction of organic compounds from representative shales and the effect on porosity. Journal of Natural Gas Science and Engineering 35, 646–660. https://doi.org/10.1016/j.jngse.2016.08.064

Espitalie, J., Deroo, G., Marquis, F., 1985a. Rock-Eval pyrolysis and its applications. Revue De L Institut Francais Du Petrole 40, 563–579.

Espitalie, J., Deroo, G., Marquis, F., 1985b. Rock-Eval pyrolysis and ots application. 2. Revue De L'Institut Francais Du Petrole 40, 755–784.

Fishman, N.S., Hackley, P.C., Lowers, H.A., Hill, R.J., Egenhoff, S.O., Eberl, D.D., Blum, A.E., 2012. The nature of porosity in organic-rich mudstones of the Upper Jurassic Kimmeridge Clay Formation, North Sea, offshore United Kingdom. International Journal of Coal Geology 103, 32–50. https://doi.org/10.1016/j.coal.2012.07.012

Furmann, A., Mastalerz, M., Bish, D., Schimmelmann, A., Pedersen, P.K., 2016. Porosity and pore size distribution in mudrocks from the Belle Fourche and Second White Specks Formations in Alberta, Canada. AAPG Bulletin 100, 1265–1288. https://doi.org/10.1306/02191615118

Guo, H., He, R., Jia, W., Peng, P., Lei, Y., Luo, X., Wang, X., Zhang, L., Jiang, C., 2018. Pore characteristics of lacustrine shale within the oil window in the Upper Triassic Yanchang Formation, southeastern Ordos Basin, China. Marine and Petroleum Geology 91, 279–296. https://doi.org/10.1016/j.marpetgeo.2018.01.013

Hackley, P.C., 2017. Application of Organic Petrology in High Maturity Shale Gas Systems, in: Geology: Current and Future Developments. pp. 3–38.

Hackley, P.C., Cardott, B.J., 2016. Application of organic petrography in North American shale petroleum systems: A review. International Journal of Coal Geology 163, 8–51. https://doi.org/10.1016/j.coal.2016.06.010

Han, Y., Horsfield, B., Wirth, R., Mahlstedt, N., Bernard, S., 2017. Oil retention and porosity evolution in organic-rich shales. AAPG Bulletin 101, 807–827. https://doi.org/10.1306/09221616069

Herbin, J.P., Fernandez-Martinez, J.L., Geyssant, J.R., Albani, A.El., Deconinck, J.F., Proust, J.N., Colbeaux, J.P., Vidier, J.P., 1995. Sequence stratigraphy of source rocks applied to the study of the Kim meridgian/Tithonian in the north-west European shelf (Dorset/UK, Yorkshire/UK and Boulonnais/France). Marine and Petroleum Geology 12, 177–194. https://doi.org/10.1016/0264-8172(95)92838-N

Huang, W.-L., 1996. Experimental study of vitrinite maturation: effects of temperature, time, pressure, water, and hydrogen index. Organic Geochemistry 24, 233–241. https://doi.org/10.1016/0146-6380(96)00032-0

Juliao, T., Suárez-Ruiz, I., Marquez, R., Ruiz, B., 2015. The role of solid bitumen in the development of porosity in shale oil reservoir rocks of the Upper Cretaceous in Colombia. International Journal of Coal Geology 147–148, 126–144. https://doi.org/10.1016/j.coal.2015.07.001

Katz, B.J., Arango, I., 2018. Organic porosity: A geochemist’s view of the current state of understanding. Organic Geochemistry 123, 1–16. https://doi.org/10.1016/j.orggeochem.2018.05.015

Keel, M.B., 2015. Organic Porosity Distribution: A Function of Aromaticity in Organic-Rich Mudrocks. University of Kansas.

Ko, L.T., Loucks, R.G., Milliken, K.L., Liang, Q., Zhang, T., Sun, X., Hackley, P.C., Ruppel, S.C., Peng, S., 2017. Controls on pore types and pore-size distribution in the Upper Triassic Yanchang Formation, Ordos Basin, China: Implications for pore-evolution models of lacustrine mudrocks. Interpretation 5, SF127–SF148. https://doi.org/10.1190/INT-2016-0115.1

Ko, L.T., Loucks, R.G., Zhang, T., Ruppel, S.C., Shao, D., 2016. Pore and pore network evolution of Upper Cretaceous Boquillas (Eagle Ford–equivalent) mudrocks: Results from gold tube pyrolysis experiments. AAPG Bulletin 100, 1693–1722. https://doi.org/10.1306/04151615092

Ko, L.T., Ruppel, S.C., Loucks, R.G., Hackley, P.C., Zhang, T., Shao, D., 2018. Pore-types and pore-network evolution in Upper Devonian-Lower Mississippian Woodford and Mississippian Barnett mudstones: Insights from laboratory thermal maturation and organic petrology. International Journal of Coal Geology 190, 3–28. https://doi.org/10.1016/j.coal.2017.10.001

Kuila, U., McCarty, D.K., Derkowski, A., Fischer, T.B., Prasad, M., 2014. Total porosity measurement in gas shales by the water immersion porosimetry (WIP) method. Fuel 117, 1115–1129. https://doi.org/10.1016/j.fuel.2013.09.073

Kuila, U., Prasad, M., Derkowski, A., McCarty, D.K., 2012. Compositional Controls on Mudrock Pore-Size Distribution: An Example from Niobrara Formation, in: SPE Annual Technical Conference and Exhibition. Presented at the SPE Annual Technical Conference and Exhibition, Society of Petroleum Engineers, San Antonio, Texas, USA. https://doi.org/10.2118/160141-MS

Kus, J., Araujo, C.V., Borrego, A.G., Flores, D., Hackley, P.C., Hámor-Vidó, M., Kalaitzidis, S., Kommeren, C.J., Kwiecińska, B., Mastalerz, M., Mendonça Filho, J.G., Menezes, T.R., Misz-Kennan, M., Nowak, G.J., Petersen, H.I., Rallakis, D., Suárez-Ruiz, I., Sýkorová, I., Životić, D., 2017. Identification of alginite and bituminite in rocks other than coal. 2006, 2009, and 2011 round robin exercises of the ICCP Identification of Dispersed Organic Matter Working Group. International Journal of Coal Geology 178, 26–38. https://doi.org/10.1016/j.coal.2017.04.013

Lafargue, E., Marquis, F., Pillot, D., 1998. Rock-Eval 6 Applications in Hydrocarbon Exploration, Production, and Soil Contamination Studies. Revue de l’Institut Français du Pétrole 53, 421–437. https://doi.org/10.2516/ogst:1998036

Lallier-Vergès, E., Bertrand, P., Tribovillard, N., Desprairies, A., 1995. Short-term organic cyclicities from the Kimmeridge Clay Formation of Yorkshire (G.B.): combined accumulation and degradation of organic carbon under the control of primary production variations, in: Organic Matter Accumulation. Springer Berlin Heidelberg, Berlin, Heidelberg, pp. 3–13. https://doi.org/10.1007/BFb0117664

Landais, P., Michels, R., Elie, M., 1994. Are time and temperature the only constraints to the simulation of organic matter maturation? Organic Geochemistry 22, 617–630. https://doi.org/10.1016/0146-6380(94)90128-7

Lazar, O.R., Bohacs, K.M., Macquaker, J.H.S., Schieber, J., Demko, T.M., 2015. Capturing Key Attributes of Fine-Grained Sedimentary Rocks In Outcrops, Cores, and Thin Sections: Nomenclature and Description Guidelines. Journal of Sedimentary Research 85, 230–246. https://doi.org/10.2110/jsr.2015.11

Lewan, M.D., 1997. Experiments on the role of water in petroleum formation. Geochimica et Cosmochimica Acta 61, 3691–3723. https://doi.org/10.1016/S0016-7037(97)00176-2

Lewan, M.D., 1993. Laboratory simulation of petroleum formation. Organic geochemistry 419–442.

Liu, Y., Xiong, Y., Li, Y., Peng, P., 2018. Effect of thermal maturation on chemical structure and nanomechanical properties of solid bitumen. Marine and Petroleum Geology 92, 780–793. https://doi.org/10.1016/j.marpetgeo.2017.12.008

Löhr, S.C., Baruch, E.T., Hall, P.A., Kennedy, M.J., 2015. Is organic pore development in gas shales influenced by the primary porosity and structure of thermally immature organic matter? Organic Geochemistry 87, 119–132. https://doi.org/10.1016/j.orggeochem.2015.07.010

Loucks, R.G., Reed, R.M., 2014. Scanning-electron microscope petrographic evidence for distinguishing organic-matter pores associated with depositional organic matter versus migrated organic matter in mudrocks. GCAGS journal 3, 51–60.

Loucks, R.G., Reed, R.M., Ruppel, S.C., Hammes, U., 2012. Spectrum of pore types and networks in mudrocks and a descriptive classification for matrix-related mudrock pores. AAPG Bulletin 96, 1071–1098. https://doi.org/10.1306/08171111061

Loucks, R.G., Reed, R.M., Ruppel, S.C., Jarvie, D.M., 2009. Morphology, Genesis, and Distribution of Nanometer-Scale Pores in Siliceous Mudstones of the Mississippian Barnett Shale. Journal of Sedimentary Research 79, 848–861. https://doi.org/10.2110/jsr.2009.092

Loucks, R.G., Ruppel, S.C., Wang, X., Ko, L., Peng, S., Zhang, T., Rowe, H.D., Smith, P., 2017. Pore types, pore-network analysis, and pore quantification of the lacustrine shale-hydrocarbon system in the Late Triassic Yanchang Formation in the southeastern Ordos Basin, China. Interpretation 5, SF63–SF79. https://doi.org/10.1190/INT-2016-0094.1

Mastalerz, M., Schimmelmann, A., Drobniak, A., Chen, Y., 2013. Porosity of Devonian and Mississippian New Albany Shale across a maturation gradient: Insights from organic petrology, gas adsorption, and mercury intrusion. AAPG Bulletin 97, 1621–1643. https://doi.org/10.1306/04011312194

Michels, R., Landais, P., Torkelson, B.E., Philp, R.P., 1995. Effects of effluents and water pressure on oil generation during confined pyrolysis and high-pressure hydrous pyrolysis. Geochimica et Cosmochimica Acta 59, 1589–1604.

Milliken, K.L., Pommer, M., Marsaglia, K.M., 2014. SEM petrography of eastern Mediterranean sapropels: Analogue data for assessing organic matter in oil and gas shales. Journal of Sedimentary Research 84, 961–974.

Milliken, K.L., Rudnicki, M., Awwiller, D.N., Zhang, T., 2013. Organic matter-hosted pore system, Marcellus Formation (Devonian), Pennsylvania. AAPG Bulletin 97, 177–200. https://doi.org/10.1306/07231212048

Misch, D., Gross, D., Hawranek, G., Horsfield, B., Klaver, J., Mendez-Martin, F., Urai, J.L., Vranjes-Wessely, S., Sachsenhofer, R.F., Schmatz, J., Li, J., Zou, C., 2019. Solid bitumen in shales: Petrographic characteristics and implications for reservoir characterization. International Journal of Coal Geology 205, 14_31.

Oschmann, W., 1988. Kimmeridge clay sedimentation — A new cyclic model. Palaeogeography, Palaeoclimatology, Palaeoecology 65, 217–251. https://doi.org/10.1016/0031-0182(88)90025-9

Pan, L., Xiao, X., Tian, H., Zhou, Q., Chen, J., Li, T., Wei, Q., 2015. A preliminary study on the characterization and controlling factors of porosity and pore structure of the Permian shales in Lower Yangtze region, Eastern China. International Journal of Coal Geology 146, 68–78. https://doi.org/10.1016/j.coal.2015.05.005

Powell, J.H., 2010. Jurassic sedimentation in the Cleveland Basin: a review. Proceedings of the Yorkshire Geological Society 58, 21–72. https://doi.org/10.1144/pygs.58.1.278

Radke, M., 1988. Application of aromatic compounds as maturity indicators in source rocks and crude oils. Marine and Petroleum Geology 5, 224–236. https://doi.org/10.1016/0264-8172(88)90003-7

Radke, M., Welte, D.H., Willsch, H., 1986. Maturity parameters based on aromatic hydrocarbons: Influence of the organic matter type. Organic Geochemistry 10, 51–63. https://doi.org/10.1016/0146-6380(86)90008-2

Ramanampisoa, L., Disnar, J.R., 1994. Primary control of paleoproduction on organic matter preservation and accumulation in the Kimmeridge rocks of Yorkshire (UK). Organic Geochemistry 21, 1153–1167. https://doi.org/10.1016/0146-6380(94)90160-0

Rawson, P.F., Riley, L.A., 1982. Latest Jurassic - Early Cretaceous Events and the “Late Cimmerian Unconformity” in North Sea Area. AAPG Bulletin 66, 2628–2648.

Reed, R.M., 2017. Organic-Matter Pores: New Findings from Lower-Thermal-Maturity Mudrocks. GCAGS journal 6, 99–110.

Reed, R.M., Loucks, R.G., Ruppel, S.C., 2014. Comment on “Formation of nanoporous pyrobitumen residues during maturation of the Barnett Shale (Fort Worth Basin)” by Bernard et al. (2012). International Journal of Coal Geology 127, 111–113. https://doi.org/10.1016/j.coal.2013.11.012

Romero-Sarmiento, M.-F., Rouzaud, J.-N., Bernard, S., Deldicque, D., Thomas, M., Littke, R., 2014. Evolution of Barnett Shale organic carbon structure and nanostructure with increasing maturation. Organic Geochemistry 71, 7–16. https://doi.org/10.1016/j.orggeochem.2014.03.008

Ross, D.J.K., Bustin, M.R., 2009. The importance of shale composition and pore structure upon gas storage potential of shale gas reservoirs. Marine and Petroleum Geology 26, 916–927. https://doi.org/10.1016/j.marpetgeo.2008.06.004

Rouquerol, J., Avnir, D., Fairbridge, C.W., Everett, D.H., Haynes, J.H., Pernicone, N., Ramsay, J.D.F., Sing, K.S.W., Unger, K.K., 1994. Recommendations for the Characterization of Porous Solids. International union of pure and applied chemistry. https://doi.org/10.1515/iupac.66.0925

Schieber, J., 2013. 13 SEM Observations on Ion-milled Samples of Devonian Black Shales from Indiana and New York: The Petrographic Context of Multiple Pore Types. AAPG 153–171.

Schieber, J., 2010. Common Themes in the Formation and Preservation of Intrinsic Porosity in Shales and Mudstones – Illustrated with Examples Across the Phanerozoic, in: Society of Petroleum Engineers. Presented at the SPE Unconventional Gas Conference, Pittsburgh, Pennsylvania USA, p. 10.

Tannenbaum, E., Kaplan, I.R., 1985. Role of minerals in the thermal alteration of organic matter—I: Generation of gases and condensates under dry condition. Geochimica et Cosmochimica Acta 49, 2589–2604. https://doi.org/10.1016/0016-7037(85)90128-0

Tian, H., Pan, L., Xiao, X., Wilkins, R.W.T., Meng, Z., Huang, B., 2013. A preliminary study on the pore characterization of Lower Silurian black shales in the Chuandong Thrust Fold Belt, southwestern China using low pressure N2 adsorption and FE-SEM methods. Marine and Petroleum Geology 48, 8–19. https://doi.org/10.1016/j.marpetgeo.2013.07.008

Tian, H., Pan, L., Zhang, T., Xiao, X., Meng, Z., Huang, B., 2015. Pore characterization of organic-rich Lower Cambrian shales in Qiannan Depression of Guizhou Province, Southwestern China. Marine and Petroleum Geology 62, 28–43. https://doi.org/10.1016/j.marpetgeo.2015.01.004

Tissot, B.P., Welte, D.H., 1984. Petroleum formation and occurrence, 2nd, rev. and enl. ed ed. Springer-Verlag, Berlin ; New York.

Appendix 1

Calculation of biomarker ratios

- MDBT: methyldibenzothiophene ratio:

$$\mathrm{MDBT}=\frac{[\text{4-MDBT}]}{[\text{1-MDBT}]}$$ (Radke et al., 1986)

- MDBT Rc % = $0.40 + 0.30\times\mathrm{MDBT} - 0.094\times\mathrm{MDBT}^2 + 0.011\times\mathrm{MDBT}^3$ (Radke, 1988).
- DPR: dimethylphenanthrene ratio:

$$\mathrm{DPR}=\frac{[\text{2,6-DMP}]+[\text{2,7-DMP}]+[\text{3,5-DMP}]}{[\text{1,3-DMP}]+[\text{1,6-DMP}]+[\text{2,5-DMP}]+[\text{2,9-DMP}]+[\text{2,10-DMP}]+[\text{3,9-DMP}]+[\text{3,10-DMP}]}$$ (Radke et al., 1986)

- DPR Rc (%) = $1.50 + 1.34\times\log_{10}\mathrm{DPR}$ (Radke, 1988).
- MPI-1: methylphenanthrene index:

$$\text{MPI-1}=\frac{1.5\times[\text{2-MP}]+[\text{3-MP}]}{[\text{Phe}]+[\text{1-MP}]+[\text{9-MP}]}$$ (Radke et al., 1986).

- MPI-1 Rc %:
  - for Rm between 0.3-1.7%, Rc = 0.70×MPI-1 + 0.22 (Boreham et al., 1988).
  - for Rm > 1.7%, Rc =-0.55×MPI-1 + 3.0 (Boreham et al., 1988).